ISTANBUL TECHNICAL UNIVERSITY ★ GRADUATE SCHOOL

CFD BASED INVESTIGATION OF DEMISTING PERFORMANCE IN HELICOPTER APPLICATIONS

M.Sc. THESIS

Furkan KESİM

Department of Defence Technologies

Defence Technologies Programme

FEBRUARY 2026

ISTANBUL TECHNICAL UNIVERSITY ★ GRADUATE SCHOOL

CFD BASED INVESTIGATION OF DEMISTING PERFORMANCE IN HELICOPTER APPLICATIONS

M.Sc. THESIS

Furkan KESİM
(514251019)

Department of Defence Technologies

Defence Technologies Programme

Thesis Advisor: Prof. Dr. Aliihsan KOCA

FEBRUARY 2026

ISTANBUL TEKNİK ÜNİVERSİTESİ ★ LİSANSÜSTÜ EĞİTİM ENSTİTÜSÜ

HELİKOPTER UYGULAMALARINDA HAD TABANLI BUGU ÖNLEME PERFORMANSININ İNCELENMESİ

YÜKSEK LİSANS TEZİ

Furkan KESİM
(514251019)

Savunma Teknolokileri Anabilim Dalı

Savunma Teknolojileri Programı

Tez Danışmanı: Prof. Dr. Aliihsan KOCA

ŞUBAT 2026

Furkan Kesim, a M.Sc. student of İTU Graduate School student ID 514251019, successfully defended the thesis/dissertation entitled "CFD BASED INVESTIGATION OF DEMISTING PERFORMANCE IN HELICOPTER APPLICATIONS", which he prepared after fulfilling the requirements specified in the associated legislations, before the jury whose signatures are below.

Thesis Advisor :	**Prof. Dr. Aliihsan KOCA** İstanbul Technical University	....
Jury Members :	**Prof. Dr. Yakup Erhan BÖKE** Istanbul Technical University	....
	Doç. Dr. Zafer GEMİCİ Yildiz Technical University	....

Date of Submission : 31.01.2026

Date of Defense : 20.02.2026

Bâkî kalan bu kubbede hoş bir sâdâ imiş,

FOREWORD

This thesis study reflects the knowledge and experience I have gained throughout my academic life and represents a concrete step toward my goal of becoming an engineer who can contribute to my country's engineering capabilities.

First and foremost, I would like to express my sincere gratitude to my thesis advisor, Prof. Dr. Ali İhsan KOCA, for his academic guidance, continuous support, and invaluable contributions throughout the research process. His mentorship has played a significant role in helping me develop a strong scientific perspective at every stage of this study.

I would also like to thank TUSAŞ for providing the necessary facilities and working environment that have made this study possible. In addition, I would like to express my gratitude to my chief engineer, Halit Terzioğlu, and all my colleagues who have contributed to this work through their technical support and motivation during the helicopter demisting analyses. Their contributions have been instrumental in ensuring the efficiency and continuity of this study.

I would like to extend my heartfelt thanks to my beloved family, Duran Kesim and Emsal Kesim, to whom I owe everything I have achieved in my life through their endless support and prayers, as well as to my sister Rumeysa Cengiz, and to my dear brother, Onur Cengiz.

I extend my deepest gratitude to my precious wife, Hilal Hastürk Kesim, who brings meaning and happiness to my life, fills my days with joy and love, is always by my side and supports me, and has made countless sacrifices throughout my thesis journey. I love you very much, my dear wife.

Finally, I offer my endless gratitude to Allah, who has created us from nothing, made us aware of existence, and honored us with knowledge. I would also like to declare, with the hope that it remains a pleasant echo in the world, that I love Allah, Prophet, and those who love Allah.

“Hüzün galîb âşıklarız, lâkin mutsuz değiliz!”

January 2026 | Furkan KESIM
Mechanical Engineer

TABLE OF CONTENTS

Page

ABBREVIATIONS

FAA	**:** Federeal Aviation Administration
CFD	**:** Computational Fluid Dynamics
CFL	**:** Courant–Friedrichs–Lewy
EWF	**:** Eulerian Wall Film
DNS	**:** Direct Numerical Simulation
LES	**:** Large Eddy Simulation
RANS	**:** Reynolds-Averaged Navier–Stokes
RH	**:** Relative Humidity

SYMBOLS

h	**:** Heat Transfer Coefficient
T	**:** Tempeature
ṁ	**:** Mass Flow Rate
Y	**:** Mass fraction

LIST OF TABLES

Page

LIST OF FIGURES

CFD BASED INVESTIGATION OF DEMISTING PERFORMANCE IN HELICOPTER APPLICATIONS

SUMMARY

In this study, the demisting performance aimed at eliminating the fogging problem on the helicopter windscreen is numerically examined, and the system behaviour under different operational conditions is evaluated using quantitative metrics. The fogging phenomenon, which directly affects pilot visibility and flight safety, is considered as a transient multiphase heat and mass transfer problem involving condensation, film formation, and subsequent film transport over the glass surface. Condensation and liquid film formation on the windscreen surface are modelled using the Eulerian Wall Film (EWF) model, which treats the wall-adjacent liquid layer as a separate phase and solves the conservation equations for mass, momentum, and energy within the film region. Meanwhile, the condensation process within the humid air domain is solved in a CFD environment over time using the species transport approach, where water vapour diffusion, convection, and phase change mechanisms are simultaneously accounted for.

Considering that evaluating demisting performance solely from a mass perspective is insufficient to fully represent optical visibility conditions, two independent performance metrics are defined to provide a more comprehensive assessment. The first metric is the total liquid film mass swept off the window surface within a specific time period, which quantifies the effectiveness of the airflow in removing condensed water from the glass. The second metric is defined as the ratio of the total viewing area to the areas where the film thickness falls below a critical threshold value, representing the optically acceptable clear region. This dual-metric framework enables the simultaneous evaluation of both physical water removal capability and visual clarity performance, thereby offering a more realistic interpretation of demisting efficiency.

The effects of operating pressure parameters, which vary depending on the inlet air flow rate, inlet air temperature, mass fraction representing humidity, and helicopter altitude, on these performance metrics are examined parametrically. Each parameter is varied within operationally realistic ranges to reflect actual flight and environmental conditions. The inlet temperature influences both the sensible heating of the glass surface and the relative humidity of the impinging airflow. The mass flow rate determines the convective heat transfer coefficient and the shear stress applied to the liquid film. The humidity parameter governs the condensation potential, while altitude affects air density and thermophysical properties, thereby modifying the overall heat and mass transfer characteristics of the system.

Regression-based correlation models are developed using the obtained CFD results in order to establish predictive relationships between the operating parameters and the defined performance metrics. These models are constructed through systematic parametric data processing, and they are validated using separate training and test data sets to ensure robustness and generalization capability. The regression results are

found to be highly consistent with CFD data, with error rates remaining within acceptable limits, indicating that the proposed reduced-order models successfully capture the dominant physical trends governing the demisting process.

The analyses reveal that air temperature is the most dominant parameter affecting demister performance, primarily due to its direct influence on saturation conditions and condensation suppression. The mass flow rate plays a decisive role in liquid film transport by increasing wall shear stress and enhancing convective heat transfer. The humidity parameter must be evaluated in conjunction with temperature, as its impact becomes critical near saturation conditions. The altitude effect is found to be limited under constant heat transfer conditions; however, it is assessed to have indirect influences depending on operational conditions, especially through variations in air density and Reynolds number.

Overall, the developed approach offers a method that enables the rapid and reliable prediction of demister performance as an alternative to computationally expensive CFD analyses. By reducing the need for repeated high-resolution simulations, this methodology significantly accelerates parametric design studies and optimization processes. Consequently, it contributes to the design, evaluation, and preliminary sizing processes of helicopter demister systems, providing both engineering insight and practical applicability for aerospace thermal management applications.

HELIKOPTER UYGULAMALARINDA HAD TABANLI DEMISTING PERFORMANSININ INCELENMESİ

ÖZET

Bu çalışmada, helikopter ön camında oluşan buğulanma problemini gidermeyi amaçlayan buğu çözme performansı sayısal olarak incelenmiş ve sistemin farklı işletme koşulları altındaki davranışı nicel performans metrikleri kullanılarak değerlendirilmiştir. Havacılık uygulamalarında kokpit görüşünün korunması, uçuş emniyetinin en kritik unsurlarından biri olarak kabul edilmektedir. Özellikle yüksek nemli atmosfer koşullarında, sıcaklık farkları nedeniyle cam yüzeyi üzerinde meydana gelen yoğuşma olgusu, pilot görüş alanını hızla azaltabilmekte ve uçuş operasyonlarını olumsuz yönde etkileyebilmektedir. Buğulanma, yalnızca yüzeyde biriken sıvı suyun oluşturduğu bir tabaka problemi değil; aynı zamanda nemli hava akışı, ısı transferi, faz değişimi ve yüzey üzerinde gerçekleşen sıvı film taşınımını içeren karmaşık bir ısı ve kütle transferi sürecidir. Bu nedenle buğu oluşumu ve giderilmesi, zamana bağlı çok fazlı bir problem olarak ele alınmalıdır. Bu çalışmada söz konusu fiziksel süreçler bütüncül bir yaklaşımla incelenmiş ve helikopter ön camı üzerinde gerçekleşen buğu çözme mekanizması sayısal akışkanlar dinamiği (CFD) yöntemleri kullanılarak analiz edilmiştir.

Pilot görüşünü ve uçuş emniyetini doğrudan etkileyen buğulanma olgusu, yoğuşma, sıvı film oluşumu ve cam yüzeyi üzerindeki film taşınımını içeren zamana bağlı çok fazlı bir ısı ve kütle transferi problemi olarak ele alınmıştır. Ön cam yüzeyinde meydana gelen yoğuşma ve sıvı film oluşumu Eulerian Wall Film (EWF) modeli kullanılarak modellenmiştir. Bu modelde, duvarla temas eden sıvı tabaka ayrı bir faz olarak ele alınmakta ve duvar yüzeyi boyunca gelişen ince film tabakasının davranışı detaylı şekilde temsil edilmektedir. Eulerian Wall Film yaklaşımı, duvar üzerindeki sıvı filmin kalınlığını, hızını ve kütlesini zamanla değişen bir alan değişkeni olarak ele almakta ve film bölgesi içerisinde kütle, momentum ve enerji korunum denklemlerinin çözülmesini sağlamaktadır. Böylece yoğuşma sonucunda oluşan sıvı suyun yüzey üzerinde nasıl yayıldığı, hangi bölgelerde biriktiği ve hava akışı etkisiyle nasıl taşındığı fiziksel olarak temsil edilebilmektedir. Bu yaklaşım, özellikle ince sıvı film tabakalarının davranışının incelenmesinde yaygın olarak kullanılan ve deneysel gözlemlerle uyumlu sonuçlar verebilen bir modelleme tekniğidir.

Aynı zamanda nemli hava bölgesindeki yoğuşma süreci, tür taşınımı yaklaşımı kullanılarak zamana bağlı bir CFD ortamında çözülmüş; su buharının difüzyonu, taşınımı ve faz değişimi mekanizmaları birlikte dikkate alınmıştır. Tür taşınımı modeli sayesinde hava içerisindeki su buharı kütle kesri alanı hesaplanabilmekte ve doyma koşullarına ulaşılan bölgelerde yoğuşma süreci başlatılabilmektedir. Bu kapsamda, gaz fazı içerisinde bulunan su buharının cam yüzeyi yakınındaki sıcaklık ve basınç koşullarına bağlı olarak sıvı faza dönüşmesi modellenmiştir. Yoğuşma sürecinin başlamasıyla birlikte yüzeyde sıvı film oluşmakta ve bu film tabakası hava akışının etkisi altında taşınarak yüzey boyunca yayılmaktadır. Bu süreçte hem gaz fazı hem de

sıvı film fazı arasında kütle ve enerji alışverişi gerçekleşmekte; böylece yoğuşma, film oluşumu ve film taşınımı mekanizmaları birbirine bağlı olarak çözümlenmektedir. Zamana bağlı çözüm yaklaşımı kullanılarak buğu oluşumu ve giderilmesinin dinamik karakteri ortaya konmuş, sistemin farklı zaman ölçeklerindeki davranışı incelenebilmiştir.

Buğu çözme performansının yalnızca kütlesel bir bakış açısıyla değerlendirilmesinin optik görüş koşullarını tam olarak temsil etmekte yetersiz kalacağı göz önünde bulundurularak iki bağımsız performans metriği tanımlanmıştır. Birinci metrik, belirli bir zaman aralığında cam yüzeyinden uzaklaştırılan toplam sıvı film kütlesi olup, hava akışının yoğuşmuş suyu camdan temizleme etkinliğini nicel olarak ifade etmektedir. Bu metrik, yüzey üzerinde oluşan sıvı film miktarının zamanla nasıl değiştiğini ve hava akışının film tabakasını ne ölçüde uzaklaştırabildiğini değerlendirmeye olanak sağlamaktadır. Özellikle yüksek debili hava akışlarında artan duvar kayma gerilmesinin film taşınımı üzerindeki etkisi bu metrik aracılığıyla incelenebilmektedir.

İkinci metrik ise toplam görüş alanının, film kalınlığının kritik eşik değerinin altına düştüğü alanlara oranı olarak tanımlanmıştır ve optik açıdan kabul edilebilir temiz bölgeyi temsil etmektedir. Bu yaklaşım, yüzey üzerinde bulunan sıvı film kalınlığının görüş üzerindeki etkisini dikkate alarak gerçekçi bir değerlendirme yapılmasını sağlamaktadır. Belirli bir eşik film kalınlığının üzerindeki bölgelerde optik bozulmanın meydana geldiği kabul edilmekte ve bu bölgeler görüş açısından olumsuz olarak değerlendirilmektedir. Buna karşılık, film kalınlığının kritik değerin altında olduğu bölgeler ise optik açıdan kabul edilebilir temiz alanlar olarak tanımlanmaktadır. Bu iki metrikli yaklaşım sayesinde hem fiziksel su uzaklaştırma kapasitesi hem de görsel netlik performansı eş zamanlı olarak değerlendirilebilmekte, böylece buğu çözme etkinliği daha gerçekçi ve mühendislik açısından anlamlı bir şekilde yorumlanabilmektedir.

Giriş hava debisi, giriş hava sıcaklığı, nemi temsil eden kütle kesri ve helikopter irtifasına bağlı olarak değişen işletme basınç parametrelerinin bu performans metrikleri üzerindeki etkileri parametrik olarak incelenmiştir. Her bir parametre, gerçek uçuş ve çevresel koşulları temsil edecek operasyonel aralıklarda değiştirilmiştir. Böylece sistemin farklı atmosfer koşulları ve operasyon senaryoları altındaki davranışı kapsamlı şekilde değerlendirilmiştir. Parametrik analiz yaklaşımı, her bir değişkenin buğu çözme performansı üzerindeki bağımsız ve birleşik etkilerinin ortaya konmasına olanak sağlamıştır.

Giriş sıcaklığı hem cam yüzeyinin duyulur ısıtılmasını hem de çarpan hava akışının bağıl nemini etkilemektedir. Daha yüksek giriş sıcaklıkları, cam yüzeyi sıcaklığını artırarak yoğuşma oluşumunu baskılamakta ve yüzey üzerinde sıvı film oluşma eğilimini azaltmaktadır. Ayrıca sıcak hava akışı, yüzey üzerinde mevcut olan sıvı filmin buharlaşmasına katkıda bulunarak buğu çözme sürecini hızlandırabilmektedir. Kütlesel debi ise taşınımla ısı transfer katsayısını ve sıvı film üzerine uygulanan kayma gerilmesini belirlemektedir. Debinin artması, yüzey üzerindeki akış hızını yükselterek duvar kayma gerilmesini artırmakta ve bu sayede sıvı film tabakasının yüzey boyunca taşınarak uzaklaştırılmasını kolaylaştırmaktadır. Aynı zamanda artan akış hızı taşınımla ısı transfer katsayısını da yükselterek yüzey ile hava akışı arasındaki enerji transferini güçlendirmektedir.

Nem parametresi yoğuşma potansiyelini kontrol ederken, irtifa hava yoğunluğunu ve termofiziksel özellikleri değiştirerek sistemin genel ısı ve kütle transferi karakteristiğini etkilemektedir. Yüksek nem oranlarında hava içerisindeki su buharı miktarı arttığından yoğuşma eğilimi güçlenmekte ve cam yüzeyinde daha kalın sıvı film tabakaları oluşabilmektedir. Bu nedenle nem parametresi özellikle doyma koşullarına yakın durumlarda buğu oluşumu üzerinde belirleyici bir rol oynamaktadır. İrtifa ise atmosfer basıncını ve buna bağlı olarak hava yoğunluğunu değiştirmektedir. Yoğunluk değişimi akış karakteristiğini ve Reynolds sayısını etkileyerek taşınım süreçlerini dolaylı biçimde değiştirebilmektedir. Bu nedenle irtifa parametresi de sistemin genel performansı üzerinde dolaylı fakat dikkate değer bir etkiye sahiptir.

Elde edilen CFD sonuçları kullanılarak, işletme parametreleri ile tanımlanan performans metrikleri arasındaki ilişkileri ortaya koymak amacıyla regresyon tabanlı korelasyon modelleri geliştirilmiştir. Bu modeller sistematik parametrik veri işleme süreciyle oluşturulmuş ve genellenebilirliklerinin sağlanması amacıyla ayrı eğitim ve test veri setleri kullanılarak doğrulanmıştır. Regresyon analizi kapsamında, CFD simülasyonlarından elde edilen geniş veri seti istatistiksel yöntemler kullanılarak analiz edilmiş ve performans metriklerini temsil edebilecek indirgenmiş mertebeli matematiksel ifadeler elde edilmiştir. Bu yaklaşım sayesinde yüksek hesaplama maliyetine sahip ayrıntılı CFD çözümlerine ihtiyaç duyulmadan sistem performansının hızlı bir şekilde tahmin edilebilmesi mümkün hâle gelmiştir.

Regresyon sonuçlarının CFD verileri ile yüksek derecede uyumlu olduğu ve hata oranlarının kabul edilebilir sınırlar içinde kaldığı görülmüştür. Bu durum, önerilen indirgenmiş mertebeli modellerin buğu çözme sürecini yöneten baskın fiziksel eğilimleri başarıyla yakaladığını göstermektedir. Aynı zamanda geliştirilen korelasyonların farklı işletme koşulları için güvenilir tahminler üretebildiği ve parametrik tasarım çalışmalarında etkin bir araç olarak kullanılabileceği ortaya konmuştur.

Analizler, buğu çözme performansını etkileyen en baskın parametrenin hava sıcaklığı olduğunu ortaya koymuştur. Bu durum, sıcaklığın doyma koşulları ve yoğuşmanın bastırılması üzerindeki doğrudan etkisinden kaynaklanmaktadır. Kütlesel debi ise sıvı film taşınımında belirleyici rol oynamakta; duvar kayma gerilmesini artırarak ve taşınımla ısı transferini iyileştirerek film uzaklaştırma sürecini hızlandırmaktadır. Nem parametresinin etkisi sıcaklık ile birlikte değerlendirilmelidir; özellikle doyma koşullarına yakın durumlarda kritik hâle gelmektedir. İrtifa etkisinin sabit ısı transfer koşulları altında sınırlı olduğu görülmekle birlikte, operasyonel koşullara bağlı olarak hava yoğunluğu ve Reynolds sayısı üzerinden dolaylı etkiler oluşturabileceği değerlendirilmiştir.

Bu çalışmada gerçekleştirilen sayısal modelleme yaklaşımının güvenilirliği ve fiziksel tutarlılığı, çözüm sürecinde kullanılan sayısal yöntemlerin dikkatli bir şekilde seçilmesi ve uygun sınır koşullarının tanımlanması ile sağlanmıştır. Zamana bağlı çözüm yaklaşımı kullanılarak yoğuşma ve sıvı film oluşumunun geçici davranışı yakalanmış, böylece buğu oluşumu ve giderilmesi sürecinin zamana bağlı evrimi ayrıntılı biçimde incelenebilmiştir. Ayrıca çözüm ağı bağımsızlığı ve zaman adımı hassasiyeti gibi sayısal doğrulama adımları dikkate alınarak elde edilen sonuçların ağ yapısına veya zaman çözünürlüğüne bağlı olarak değişmediği doğrulanmıştır. Bu sayede elde edilen akış, sıcaklık ve film kalınlığı dağılımlarının fiziksel olarak anlamlı ve güvenilir olduğu ortaya konmuştur. Özellikle cam yüzeyi yakınındaki sınır tabaka bölgesinde meydana gelen sıcaklık ve nem gradyanlarının doğru şekilde temsil edilmesi, yoğuşma sürecinin doğru modellenmesi açısından kritik önem taşımaktadır. Bu bağlamda kullanılan modelleme yaklaşımı, hem gaz fazındaki taşınım süreçlerini hem de yüzey üzerinde gelişen sıvı film davranışını eş zamanlı olarak çözebilme yeteneği sayesinde buğu oluşumu ve buğu çözme mekanizmalarının fiziksel doğasını kapsamlı bir şekilde temsil etmektedir.

Sonuç olarak geliştirilen yaklaşım, hesaplama maliyeti yüksek CFD analizlerine alternatif olarak buğu çözme performansının hızlı ve güvenilir şekilde tahmin edilmesini sağlayan bir yöntem sunmaktadır. Yüksek çözünürlüklü simülasyonlara olan ihtiyacı azaltarak parametrik tasarım ve optimizasyon çalışmalarını önemli ölçüde hızlandırmaktadır. Böylece bu metodoloji, helikopter buğu çözme sistemlerinin tasarım, değerlendirme ve ön boyutlandırma süreçlerine hem mühendislik içgörüsü hem de pratik uygulanabilirlik açısından katkı sağlamaktadır. Ayrıca geliştirilen sayısal modelleme yaklaşımı ve regresyon tabanlı indirgenmiş modeller, benzer yoğuşma ve buğu giderme problemlerinin incelendiği diğer mühendislik uygulamalarına da uyarlanabilecek potansiyele sahiptir.

1. INTRODUCTION

Helicopters are used in many critical operations such as search and rescue, military missions, emergency medical services, and civil transport. One of the most important factors directly affecting the pilot's situational awareness and flight safety during these operations is the quality of vision provided through the cockpit windscreen. Condensation and fogging can occur on the helicopter windscreen, particularly in conditions of low temperature, high humidity and instantaneous environmental changes, which can seriously restrict the pilot's vision.

Visibility loss in helicopter operations, especially during critical phases such as landing, descent and low-altitude flights, poses a significant safety risk. The thin film of liquid that forms on the windshield causes light refraction and impaired visibility; the effectiveness of demisting/defogging systems is crucial in this regard. However, the performance of these systems varies depending on the flow rate, temperature, humidity content of the intake air, and flight conditions. Therefore, evaluating demist performance based on a single parameter is insufficient; a multi-parameter approach is required.

The performance evaluation of demisting systems traditionally involves experimental studies. However, such studies are both costly and limited in scope due to the vast parameter space. At this point, numerical methods offer a powerful tool that enables the systematic investigation of different operating conditions. In particular, Computational Fluid Dynamics (CFD) methods enable the physical modelling of condensation on window surfaces, liquid film formation, and the time-dependent transport of this film.

In this thesis study, the fogging phenomenon occurring on the helicopter windscreen and the process of fog removal have been investigated numerically. The liquid film behaviour on the windscreen surface is modelled using the Eulerian Wall Film (EWF) model, while the condensation process is addressed using the species transport approach. Using the obtained CFD results, two separate performance metrics that quantitatively define demisting performance are determined. These are: the total liquid film mass removed from the surface within a certain period of time and the visible area clearance ratio, defined as the ratio of the total area of regions falling below the critical film thickness.

The relationship between the specified performance metrics and parameters such as operating pressure, which varies depending on the inlet air flow rate, temperature, humidity, and flight altitude, is examined parametrically. Furthermore, regression models based on CFD results are developed to predict demister performance in terms of these parameters. These developed regression models are verified by comparing them with CFD results and are shown to provide high compliance within acceptable error levels. This approach enables the rapid and reliable prediction of demister performance for different operating conditions.

1.1. Purpose of Thesis

The primary objective of this thesis is to investigate the performance of demisting systems designed to eliminate fogging on helicopter windshields using numerical methods and to quantitatively evaluate system behaviour under different operational conditions. Pilot visibility is a critical component of flight safety in helicopter operations, and condensation and liquid film formation on the windscreen surface can adversely affect visibility. Therefore, it is necessary to physically model the demisting process correctly and define its performance using reliable metrics.

Another objective of the thesis is a systematic study of the fundamental input parameters affecting demisting performance. Within this scope, the effects of parameters such as air flow rate, air temperature, mass fraction representing humidity, and operating pressure varying with helicopter altitude on demisting performance are investigated parametrically. Regression models are developed using data obtained from analyses representing different flight conditions, with the aim of predicting demisting performance in terms of these parameters.

Finally, the developed regression models are verified by comparing them with CFD results, demonstrating high agreement within acceptable error levels. This enables the presentation of an approach that allows for the rapid and reliable prediction of demisting performance under different operating conditions, serving as an alternative to comprehensive and computationally expensive CFD analyses.

1.2. Literature Review

There are numerous numerical and experimental studies in the literature aimed at modelling condensation and the behaviour of liquid films forming on surfaces. These studies primarily focus on heat and mass transfer mechanisms, condensation models, and surface condensation problems in various engineering applications. However, a review of the literature revealed no specific study that addresses the removal of fogging on helicopter windshields, evaluates demisting performance over time using quantitative metrics, and is based on helicopter operating conditions. This indicates that the present study targets a gap in the literature and necessitates a numerical investigation of demisting performance specific to helicopters.

1.2.1. Condensation physics

1.2.1.1. Condensation models

The majority of atmospheric (moist) air consists of dry gases, but it also contains a certain amount of water vapour. This water vapour remains in the gaseous phase unless environmental conditions change; however, the moist air temperature decrease below the dew point of the water vapour, the vapour loses its stable state and transforms into the liquid phase. This process is called as condensation phenomenon. Physically, during condensation, the kinetic energy of water molecules in the gaseous phase decreases and intermolecular attractive forces become dominant. During this process, energy release (latent heat release) occurs and plays an important role in heat transfer.

Essentially, condensation occurs through two different physical mechanisms, as shown in Figure 1.1: These are homogeneous condensation and heterogeneous condensation. Homogeneous condensation is the formation of the liquid phase from vapour without any surface effect within the volume. This type of condensation generally occurs under conditions of high saturation and excessive cooling. Random collisions between molecules result in the formation of small clusters; however, these clusters remain unstable and re-evaporate unless they reach a certain critical size. For this reason, homogeneous condensation is rarely observed in nature or in engineering applications and occurs more frequently under specific thermodynamic conditions, such as in steam turbines or cloud formation processes.

Heterogeneous condensation occurs when vapour contacts a solid surface. In this case, the surface temperature must be below the dew point of the contacting gas mixture.

The surface creates an energetically stable attraction point for water molecules, causing vapour molecules to adhere to the surface and initiate the liquid phase. Examples of this type include fogging on windows in everyday life, condensation on metal surfaces, or fog formation on helicopter cockpit windows. Heterogeneous condensation is directly influenced by many parameters, such as the surface temperature, roughness, contact angle, and surface energy.

In heterogeneous condensation, two distinct regimes occur depending on the behaviour of the liquid phase formed on the surface: dropwise and filmwise condensation. In dropwise condensation, water vapour adheres to the surface in the form of independent droplets. Each droplet remains on the surface until it grows large enough, then merges with others or detaches from the surface due to gravity. Throughout this process, a large portion of the surface remains in direct contact with the vapour in the air, resulting in a higher heat transfer coefficient compared to filmwise condensation. Although dropwise condensation is efficient in terms of heat transfer, it is difficult to maintain for long periods. As the droplets merge, the surface quickly transforms into a continuous liquid film, transitioning to the filmwise condensation regime. Therefore, dropwise condensation is considered a short-lived and unstable state. In filmwise condensation, water vapour adheres to the surface, forming a continuous liquid film. This film completely covers the surface and, over time, flows along the surface due to the effects of gravity or surface tension. However, this liquid film creates an additional heat transfer resistance between the surface and the vapour. Since heat must be transferred from the vapour phase through the liquid film to reach the surface, the heat transfer coefficient in filmwise condensation is lower than in the dropwise regime. On the other hand, filmwise condensation is stable and predictable, making it much easier to model computationally in engineering applications. Filmwise condensation is predominantly observed on wettable (hydrophilic) surfaces such as metal or glass.

The interest area of this thesis is the heterogeneous filmwise condensation process occurring on helicopter cockpit windows. This is because cockpit windows are generally hydrophilic in nature, and the condensation forming on the surface develops as a continuous thin liquid film. This film layer impairs optical transparency, obstructing the pilot's vision. Consequently, the physics addressed in demisting analyses encompasses the formation of this film layer, its evaporation through heat transfer, and its removal by airflow.

In conclusion, condensation physics is a complex heat and mass transfer phenomenon that occurs alongside phase transition. Accurately modelling the dominant mechanism in this process, filmwise condensation physics, is fundamental to correctly analysing helicopter demisting performance.

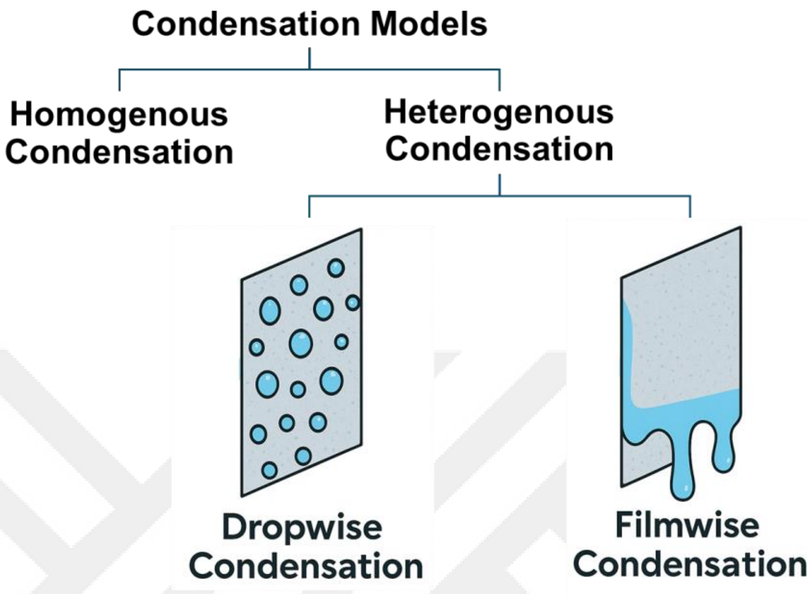

Figure 1. 1 : Condensation models

1.2.1.2. Heat and mass transfer mechanism in condensation

Condensation is the phase change of a fluid in the vapour to a liquid condition when its temperature falls below the saturation temperature due to a cold surface touching it. During this transformation, latent heat of vaporization is released as the fluid transitions from the gas to liquid phase, and this heat energy is transferred to the cold surface. Since condensation is a process involving phase change, it causes fluid movements such as droplets flowing off the surface; therefore, condensation can also be considered a type of convective heat transfer process [1].

Depending on the shape of the condensed vapour accumulating on the cold surface, two different condensation modes are observed: film condensation and droplet condensation. The heat and mass transfer mechanisms occurring in these two cases exhibit significant differences. The physics of interest in this study is film condensation. During condensation in a film, the condensing liquid surface increases, forming a liquid film layer that exhibits continuity on the surface. This film, formed under the influence of gravity, flows downwards along the surface, and its thickness gradually increases as new vapour condenses onto it. This liquid film slows down heat transfer by forming a thermal resistance layer between the vapour and the cold wall surface. This phenomenon is referred to in the literature as film resistance. Heat transfer from the condensing vapour to the film surface occurs by convection, while heat transfer from within the film to the wall occurs by conduction. Due to the two-stage heat transfer, the total heat transfer rate in film condensation is significantly lower than in droplet condensation [2].

The first extensive theory describing the film condensation process on a vertical surface in laminar flow was developed through Nusselt's classical analysis, published in 1916. This analysis is based on the heat transferred by conduction through a thin liquid film flowing under the influence of gravity and provides analytical solutions for quantities such as film thickness and average heat transfer coefficient. According to Nusselt's laminar film condensation analysis, the average heat transfer coefficient h on a horizontal surface is expressed as follows:

$$\bar{h} = 0.943\left(\frac{\rho_l(\rho_l - \rho_v)gh_{fg}k_l^3}{\mu_l L \Delta T}\right)^{0.25} \tag{1.1}$$

In this equation, the subscript l denotes the liquid phase, while v denotes the vapour phase. Here, ρ represents density, g represents gravitational acceleration, h_{fg} represents latent heat of vaporisation, k represents thermal conductivity, and μ represents dynamic viscosity, L represents the characteristic length.

This relationship clearly demonstrates that the heat transfer coefficient depends on the physical properties of the fluid, such as density, viscosity, surface tension, and difference of temperature. In practical systems, however, deviations from this theoretical solution may occur due to factors such as surface ripples, turbulence, and surface roughness. Nevertheless, this Nusselt analysis serves as a starting point for defining the fundamental engineering correlations of film condensation.

In many practical condensation situations, the condensable vapour is not entirely pure; for example, water vapour in the atmosphere is usually mixed with a certain amount of non-condensable gas. When the condensation process occurs within this mixture of gases, a gas boundary layer forms near the condensation surface due to the accumulation of these non-condensable gases [3]. This layer reduces the partial vapour pressure at the surface; consequently, it is only possible for fresh vapour to reach the condensation interface by diffusion, that is, by mass transfer. Diffusion in this boundary layer becomes the major mechanism limiting the condensation rate.

In this process, mass transfer is described by Fick's Law of Diffusion:

$$j'' = -\rho D \frac{dy_v}{dx} \tag{1.2}$$

In this equation, j″ represents condensate mass flux per unit area, D represents mass diffusivity, y_v represents mass fraction of vapor, x normal direction of the plate.

This dependence shows that the vapour is transported to the surface by diffusion along the concentration gradient. A low concentration gradient or thickening of the boundary layer reduces the dy_v/dx term and therefore reduces the amount of vapour transported by diffusion.

Similar to mass transfer, heat transfer during condensation can also be expressed in terms of the total heat flux:

$$q'' = h \cdot \Delta T \tag{1.3}$$

$$q'' = j'' \cdot h_{fg} \tag{1.4}$$

The second equation expresses the latent heat flux carried by the mass flow accumulating on the surface. When these two equations are considered together, a solution is required for thermal equilibrium in systems having multiple heat and mass transfer. In such systems, vapour condensation has a two-way effect as both a heat transfer process and a mass transfer process.

Consequently, the presence of a small amount of non-condensable gas in the vapour significantly reduces the condensation rate and seriously decreases the overall heat transfer coefficient [1, 2].

1.2.1.3. Psychrometric principles and dew point temperature

Atmospheric air (humid air) is a mixture of dry air and a certain amount of water vapour. Psychrometry is the discipline that studies the thermodynamic properties of this mixture and plays an important role in heating, cooling, ventilation, air conditioning, and condensation applications [1].

The behaviour of humid air creates a thermodynamic system in which multiple variables, such as pressure, temperature and water vapour content, interact simultaneously. Therefore, parameters that relate this complex system to each other, such as the physical state of moisture in the air and the dew point, are generally examined using a psychrometric chart. A psychrometric chart is a graph that presents all the fundamental properties of moist air for a given total pressure (usually atmospheric pressure). The thermophysical properties of the humid air on the psychrometric chart are shown in Figure 1. 2.

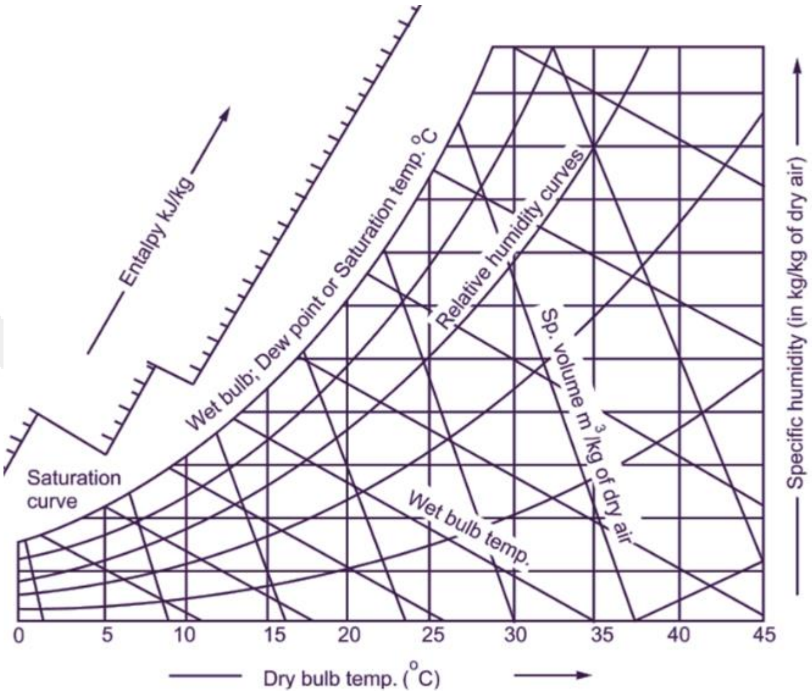

Figure 1. 2 : Thermophysical properties on psychrometric chart

In the psychrometric diagram shown in Figure 1. 2, the horizontal axis represents the dry-bulb temperature and the vertical axis represents the specific humidity while the curved boundary line represents the saturation curve of water. Each point on this curve indicates the temperature-humidity combination at which water vapour is saturated. The area between the saturation curve and the horizontal temperature lines represents air with a specific relative humidity value. Relative humidity is the ratio of the water vapour content of the mixture to the maximum (saturated) vapour quantity possible at the same temperature and is a primary indicator of whether condensation will take place [4].

The surface temperature must be below the dew point temperature of the water vapour in the mixture for condensation to occur. The dew point temperature is defined as the temperature at which the water vapour in moist air becomes saturated and begins to condense, and it depends only on the partial pressure of water vapour in the mixture.

As a result, the dew point temperature of moist air is a unique thermodynamic parameter that differs from both the dry-bulb temperature and the wet-bulb temperature.

$$T_{dp} = T_{sat@P_v} \tag{1.5}$$

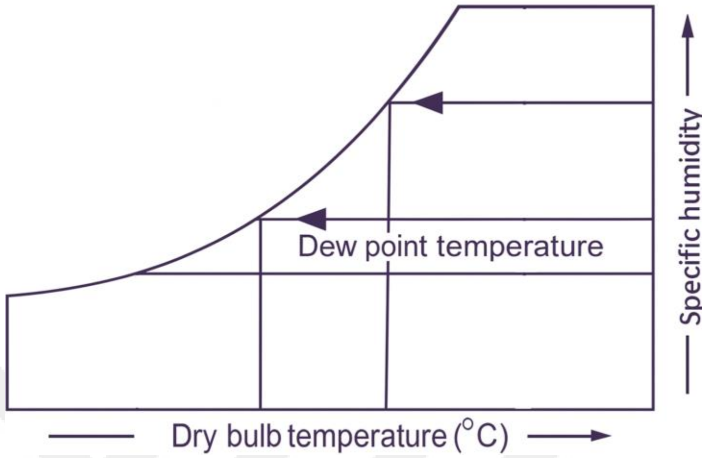

Figure 1. 3 : Dew point tempereature on psychrometric chart

As shown in Figure 1. 3, the constant specific humidity line on the psychrometric chart, the point where it intersects with the saturation curve gives the dew point temperature. Therefore, two different air with the same humidity ratio have the same dew point temperature, even if their temperatures are different. This fact shows that condensation is a process determined not only by temperature but also by humidity content in engineering applications. When the temperature of a surface falls below the dew point temperature, the air in contact with the surface can not keep the water vapour in the gas phase, and the vapour partial pressure exceeds the saturation pressure. In this situation, the vapour becomes liquid, and condensation begins. Therefore, the basic criteria for condensation is a surface temperature lower than the dew point temperature.

The dew point temperature also directly affects the amount of condensation, the timing of condensation , and the film thickness development on the surface. For example, in helicopter cockpit windows, if the cabin humidity is high, the dew point temperature will also be high. In this scenario, even slight cooling of the window can initiate condensation. Similarly, when analysing ‘fogging’ problems that occur on automotive headlights or window surfaces using psychrometric charts, important information can be obtained regarding surface design and ventilation strategies [5].

The standard psychrometric diagram prepared by ASHRAE corresponding to an atmospheric pressure of 101,325 Pa (sea level) is given in Figure 1. 4. The diagram allows for a comprehensive assessment by incorporating the fundamental thermodynamic properties of moist air, such as dry bulb temperature, wet bulb temperature, relative humidity, specific volume, enthalpy, and moisture ratio, into a single graph. This chart is a widely used reference tool in engineering applications for analysing condensation, humidity control, and air conditioning processes.

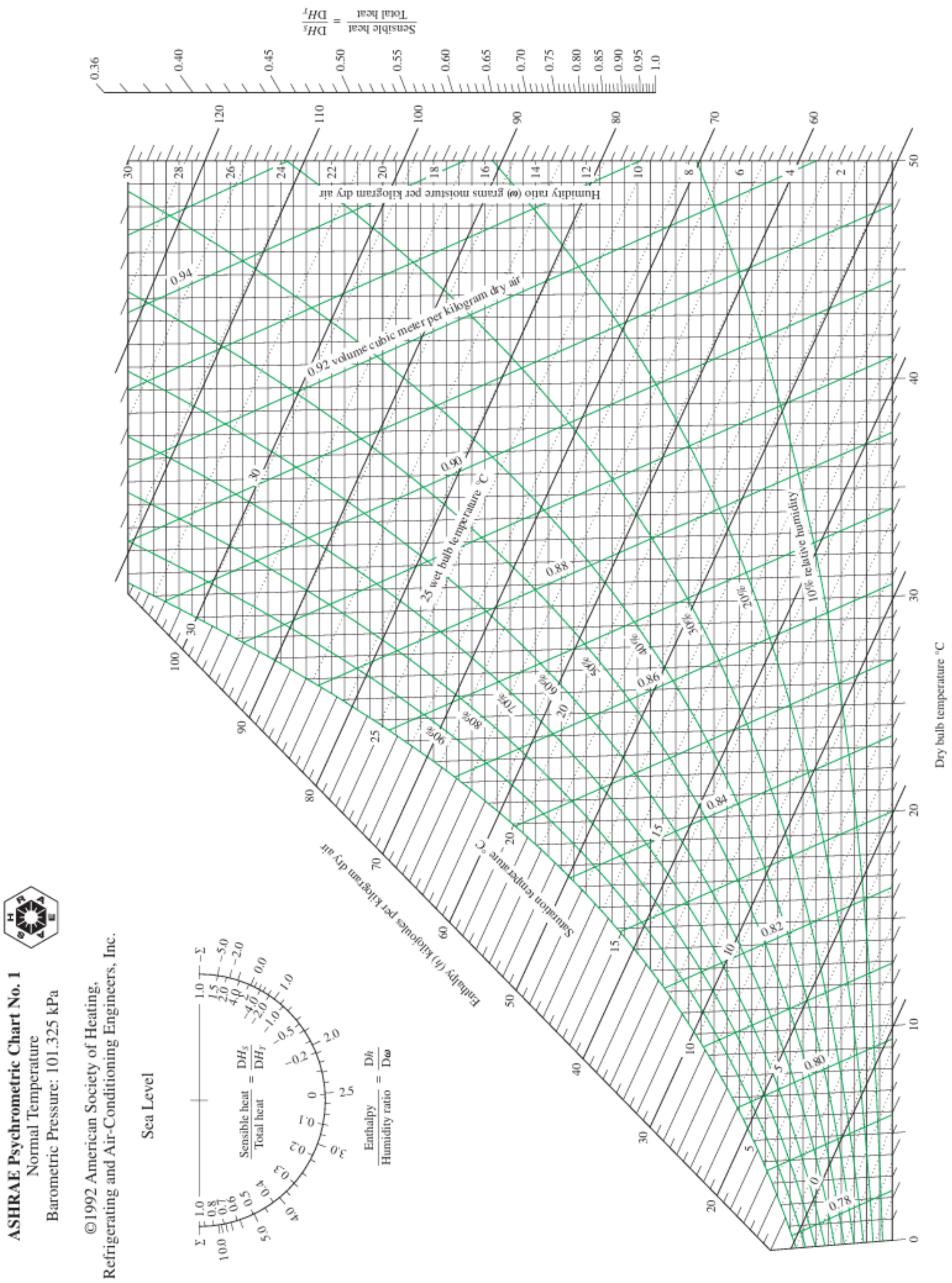

Figure 1. 4 : ASHRAE psychrometric chart at sea level [6]

1.2.2. Application fields of wall condensation

The phenomenon of wall condensation occurs in many engineering systems and sectors. While this phenomenon provides a preferred heat transfer mechanism in some cases, on the other hand, it appears as undesired fogging, negatively affecting system performance or visibility. The application areas of the condensation phenomenon range widely, from passive cooling systems in nuclear reactors to building climate control and cooling electronic devices, from fogging problems in automotive glass and headlights to maintaining cockpit visibility in aviation. Below, the main application areas of condensation on walls and some studies from the literature in these areas are summarised.

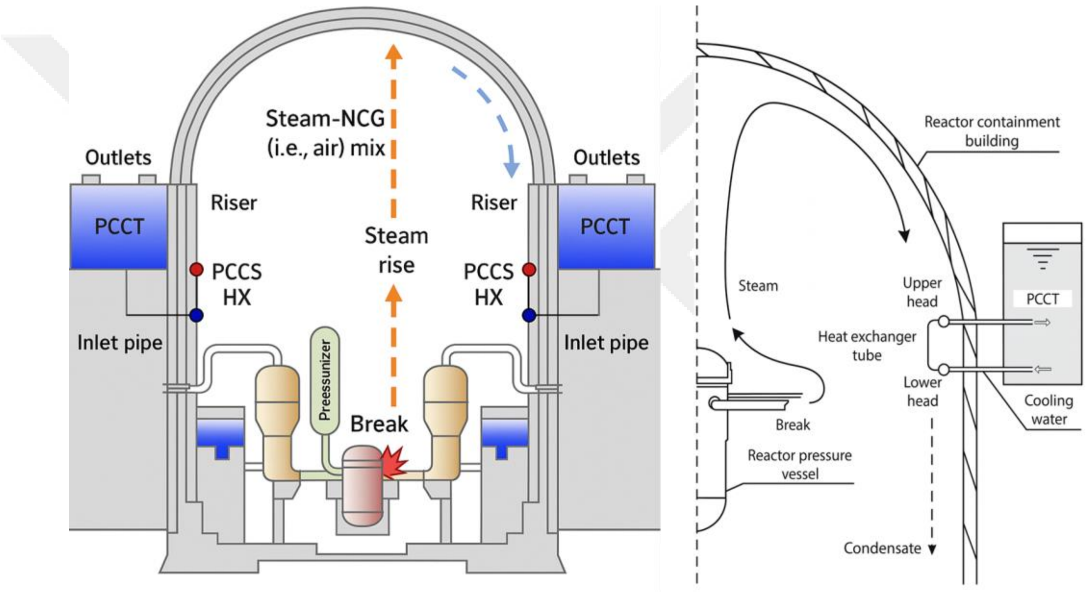

Figure 1. 5 : Schematic diagram of passive containtment cooling system [9]

Condensation plays a critical role in the safety systems of nuclear power plants. In potential accident scenarios, steam released inside the reactor containment condenses upon contact with cold wall surfaces, thereby passively transferring heat energy to the walls and dissipating it to the external environment. The literature shows that existence of non-condensable gases in this process reduces condensation efficiency and limits heat transfer. The schematic of this system is given in Figure 1. 5 [7]. Developed CFD models for predicting condensation behaviour are validated using data obtained from experimental setups such as CONAN and COPAIN, and studies are ongoing on condensation processes inside reactor containments. For example, in the international SARNET benchmark study conducted by Ambrosini et al., different CFD codes were compared to test the reliability of wall condensation models, and computational tools in this field were improved [8]. Consequently, the effectiveness of wall condensation in nuclear applications is critical for safety, and it is necessary to accurately model condensation mechanisms and develop correlations consistent with experiments.

Another area where condensation physics is observed is in the cooling of high-performance electronic systems using phase-change two-phase heat transfer mechanisms. Particularly in components that generate intense heat, devices such as heat pipes and vapour chambers effectively dissipate heat through the evaporation/condensation cycle of the fluid inside them. In these elements, a coolant fluid inside a closed chamber transitions to the vapour phase in the hot region where heat is generated; the resulting vapour is transported to the cold region of the device, where it condenses upon contact with the walls. The latent heat released during condensation is transferred outside the device, and the condensed liquid returns to the hot end through capillary structures. This cycle provides very high effective heat conductivity, protecting electronic components from overheating. The success of this type of two-phase cooling element depends on the condensation process occurring continuously. The presence of non-condensable gas inside negatively affects the phase transition. According to Cengel, even a 0.5% volume mixture of air in a closed vapour circuit can reduce the heat transfer coefficient achieved during condensation by approximately five times [1]. For this reason, heat pipes and similar devices are filled under vacuum during the production stage to completely remove air.

Condensation and humidity control are fundamental principles in heating, ventilation, and air conditioning (HVAC) systems. Particularly in humid conditions, the cooling coil pipes in an air conditioner or dehumidifier serve to cool the air below the dew point, thereby condensing the water vapour into liquid form. This reduces the relative humidity of the air, preventing condensation from forming on surfaces inside buildings or vehicle cabins. Considering condensation in HVAC design is important for indoor air quality and comfort. For example, a numerical study conducted on a train cabin climate control system using internal air recirculation showed that the formation of a condensation film on the cabin's internal surfaces significantly affected the cabin's temperature and humidity distribution [9].

Condensation application areas are examined in also automotive industry. Temperature and humidity differences between the interior and exterior of road vehicles, particularly in cold weather, cause fogging on vehicle windshields, as shown in Figure 1.6 a. When warm, humid cabin air meets a cold windshield surface, the water vapour condenses as a thin film or microscopic droplets on the windshield when it falls below the dew point temperature. The liquid layer on the windshield refracts light and restricts the driver's view of the road. To correct this restricted view, vehicles use defrost/demist systems designed to remove fogging. In a typical vehicle HVAC system, a stream of warm and relatively dry air is directed towards the windshield to evaporate and remove the condensed water film on the surface [10]. Since defogging performance is critical for passenger safety and comfort, both experimental and computational studies are being conducted to determine optimal airflow strategies. Mehdipour et al. (2017) simulated a full-scale passenger car cabin using CFD and tested various ventilation configurations, demonstrating that directing warm air from the lower part of the windshield and extracting from specific points clears fog the fastest [10]. Similarly, Yang, Huang and Zhao investigated the effect of different air-conditioning settings on the condensation film on the surface in a numerical study conducted using the Eulerian Wall Film approach on a truck cabin model. [11].

Another area in the automotive industry where wall condensation physics is observed is inside vehicle headlamps, as shown in Figure 1.6 b. Today, LED headlights produce less heat, so the air inside the headlight can easily cool down and cause fogging on the outer transparent cover of the headlamp. The presence of water on the inner surface of the headlight reduces its light transmission, diminishes lighting performance, and negatively impacts traffic safety. For this reason, various defogging solutions are applied to prevent condensation in headlights. Methods such as adding small ventilation channels to the headlight housing, placing moisture-absorbing packets, and applying anti-fog coatings to internal surfaces are common. In recent years, CFD-based simulations have been used to understand the condensation and drying processes inside headlights. For example, Guzej and Zachar (2019) created a 3D numerical model of a car headlamp and simulated the air circulation, heat transfer, and condensation-evaporation cycle inside the headlamp [5]. By validating the numerical model through experimental demisting tests conducted on a headlamp prototype, the effectiveness of different ventilation strategies in demisting was evaluated. This study demonstrates that numerical tools are useful for detecting and eliminating potential condensation problems in headlamp design in advance. Consequently, managing condensation in automotive lighting systems has become a critical design parameter for user safety.

a. **Windshield Fogging** b. **Headlamp Fogging**

Figure 1. 6 : Fogging applications in automotive industry

In aviation applications, fogging caused by condensation is also a serious problem, particularly on the cockpit windshields of aeroplanes and helicopters, as shown in Figure 1.7. The pilot's cabin usually has a large front windscreen that is in contact with the outside environment, and when outside temperatures combine with the humidity inside the cabin, condensation can form on the windscreen surface in the form of mist. As mentioned earlier, this fog can restrict the pilot's vision, which is critical for flight safety. For this reason, various anti-fog solutions have been developed for aircraft. A method frequently used in fixed-wing aircraft is to apply electrical heating by placing a transparent conductive film layer on the inner surface of the cockpit windows; this keeps the window surface above the dew point, preventing condensation. In helicopters, hot air blowing systems called demisters are generally used. The helicopter's cabin heating/air conditioning system directs hot, dry air from nozzles over the windshield surface to disperse the fog.

Among the wide range of applications where wall condensation physics is encountered, this thesis focuses on the phenomenon of fogging on the windscreen, which directly affects flight safety in helicopter operations. Accordingly, the following sections will examine the behaviour of the film layer formed by wall condensation on helicopter windshield and the removal of the resulting fog.

Figure 1. 7 : Fogging applications in aviation industry

1.2.3. Demisting visibility parameters in literature

In removal fog on the helicopter windshield projects, a critical view area is defined. The critical field of view is the mandatory viewing area defined by specific geometric and angular limits, where a pilot's vision must not be obstructed under any circumstances in order to perform their flight safely. This area is established based on the eye position, viewing angle, and geometric projections of the windshield surfaces determined according to the operational requirements of the relevant aircraft. The definition of this area is vital importance for ensuring safe flying, evaluating vision-limiting conditions such as fog, and determining the reference areas for analysing the performance of defog systems.

Most of the research on this concept has originated in the automotive industry. International standards for automotive windscreens classify the critical viewing area into zones A, B, and C. In this classification, zone A is the driver's primary viewing area and is considered the most critical zone in terms of safety. It is a legal requirement that this entire zone be completely free of fog, dirt, and obstructions. For example, in the ECE R43 and ECE R125 standards and FMVSS 104-FMVSS 103 regulations, 100% cleaning of the A zone is obligatory; whereas a lower percentage is sufficient for the broader B zone, and generally at least 70–80% cleaning is sufficient for the C zone. These areas are also used as performance criteria in automotive-focused demisting studies in the literature; for example, Mehdipour et al. reported that 80% of area A and 100% of the narrower critical area C must be cleared [10]. Therefore, the automotive literature addresses critical viewing areas within a sophisticated framework, both in terms of geometric standardisation and performance evaluation.

However, in the aviation industry, there is no comprehensive standardised study corresponding to the A–B–C area classification used in the automotive industry. The visibility requirements in helicopter and aeroplane cockpits are based more on general visibility criteria and specific angle requirements in the context of flight safety. Specifically, the 'CFR-29.773 Pilot Compartment View [12]' section indicates that rotorcraft pilots must have adequate visibility, but does not propose area-based zoning as in the automotive industry. This section provides a general definition aimed at ensuring the necessary visibility for helicopter pilots during typical operational tasks.

The most reliable guide for the technical definition of the critical viewing area in aviation is the angle of view criteria in FAA AC 25.773-1 – Pilot Compartment View Design Considerations [13]. However, this document was created for fixed-wing aircraft, it also serves as a basis for determining the viewing requirements in rotorcraft operations. According to AC 25.773-1, using the eye point as a reference, the pilot must have an vision field at ±40° left–right and approximately +35° up / –17° down. These angle envelopes and tolerances form the basis of the geometric and operational framework of the critical field of view in aviation.

Consequently, while the automotive industry defines critical fields of view in detail based on A–B–C zones and percentage performance requirements, the aviation sector focuses more on angular field of view requirements. In this study, the critical field of view on helicopter windows was determined by evaluating the conceptual approach of automotive zones in the literature, the basic field of view requirements specified for helicopters in CFR-29.773, and the angle-based field of view criteria defined in AC 25.773-1. Thus, a critical field of view definition specific to the aviation field, suitable for the helicopter's mission profile and usable in demisting analyses, has been obtained. The final geometric appearance of this critical view area in the helicopter demist analyses is presented in Figure 1. 8.

There is no specific time period specified in aviation standards for defogging the critical view area. Relevant aviation documents only define angular visibility requirements and do not provide criteria for demisting time. In the literature, automotive, train, and various cabin HVAC studies consider clearing the critical field of view significantly within the first 30–90 seconds to be sufficient for performance. Considering these datas, this study has determined that clearing the critical field of view within 60 seconds is an acceptable criterion.

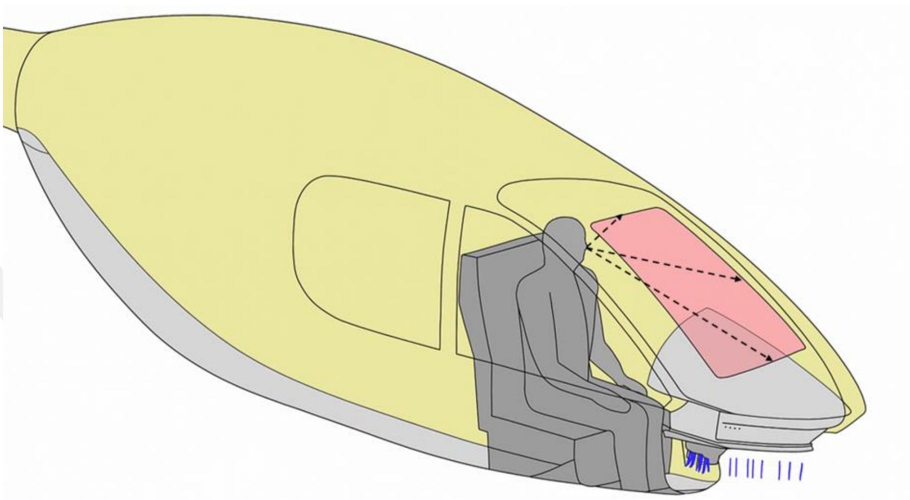

Figure 1. 8 : Critical view area of the helicopter analyses

The literature has reported several experimental limits regarding when the condensation film on the surface completely obstructs visibility or when visibility returns to an acceptable level. In the experimental-numerical defogging study conducted by Hassan et al. [14], it was found that the windscreen was considered optically “transparent” when the thickness of the condensation film on the windscreen fell below 5 µm. In this thesis, a film thickness of $h \leq 5$ µm in the critical field of view was also taken as the reference point for restoring pilot visibility.

2. METHODOLOGY

In this thesis study, numerical modelling approach is preferred to investigate detailed multi-phase flow processes involving surface condensation. During the modelling process, fluid motion, temperature change, turbulence effects, and condensation-evaporation film behaviour are considered together. ANSYS Fluent software package is used for the numerical solution of all these physical processes.

2.1. Mathematical and Physical Modelling

The solutions are based on the Finite Volume Method. In this method, the conservation equations—continuity, momentum, and energy—are solved for each cell using the control volume approach. Second-order discretisation is preferred in the numerical solutions, with convergence criteria and solution reliability tested for various grid structures and time steps. The condensation film formed on the wall surface is modeled by the Eulerian Wall Film model. This method provides the ability to model both condensation-evaporation phase transitions and film movements.

2.1.1. Governing equations

The behaviour of fluids is defined by expressing fundamental physical laws in differential form, and these mathematical expressions are called governing equations, which form the basis of computational fluid dynamics. These equations are derived from the principles of conservation of mass, momentum, and energy under the assumption of fluid continuity, and describe the time and position-dependent changes in fundamental quantities such as velocity, pressure, density, and temperature in the flow field. Combined, these conservation equations, known as the Navier–Stokes equations, form the theoretical foundation for all CFD applications, ranging from low-speed, incompressible flows to complex, turbulent, and compressible flow regimes. Therefore, the accuracy and physical correctness of a numerical solution directly depend on these governing equations to be modelled correctly and solved using appropriate numerical methods.

The conservation of mass (continuity) equation is based on the law of mass conservation established by Lavoisier and indicates that the total mass in the system remains unchanged. In general form, the continuity equation is expressed as follows:

$$\frac{\partial \rho}{\partial t} + \nabla \cdot (\rho \vec{V}) = 0 \tag{2.1}$$

where ρ is the fluid density; t is the time and $\vec{V}$ is the velocity vector of the fluid.

If the flow is incompressible (ρ=constant), the continuity equation can be written more simply as follows:

$$\nabla \cdot \vec{V} = 0 \tag{2.2}$$

This statement indicates that the flow entering and leaving a control volume is equal, meaning that the divergence of the velocity field of a constant-density fluid is zero.

The conservation of momentum equation is based on Newton's second law of motion. According to this law, the total net force acted on a fluid particle is equal to the time-dependent change in the particle's momentum. In fluid mechanics, these forces are divided into two main classes: surface forces acting through the control surface and body forces acting on the entire volume of the fluid in accordance with its mass. Surface forces consist of pressure forces and viscous stresses, while body forces include field forces such as gravity, electromagnetic forces, or inertial forces. The combined effect of these two force groups is converted into a differential form and the Navier–Stokes equations are obtained:

$$\rho \frac{\partial \vec{V}}{\partial t} + \rho (\vec{V} \cdot \nabla) \vec{V} = -\nabla p + \nabla \tau + \vec{F}_{body} \tag{2.3}$$

Here, $-\nabla p$ denotes normal surface forces derived from pressure, $\nabla \tau$ denotes tangential surface forces due to viscous stresses, and $\vec{F}_{body}$ represents the body forces like gravity. Thus, the momentum equation becomes the fundamental conservation expression that describes how the velocity field in the fluid develops under pressure gradients, viscous forces, and body forces.

If the flow is incompressible (ρ=constant), the momentum equation can be written more simply as follows:

$$\rho \left[\frac{\partial \vec{V}}{\partial t} + (\vec{V} \cdot \nabla) \vec{V} \right] = -\nabla p + \mu \nabla^2 \vec{V} + \vec{F}_{body} \tag{2.4}$$

where μ is the dynamic viscosity of the fluid.

The energy conservation equation is derived by applying the first law of thermodynamics to fluids and defines how the total energy of a fluid particle changes with time. According to this theory, the total energy change in the control volume is the result of the total effect of the energy flux carried by convection, heat conduction, the work done by viscous stresses on the flow, and any additional energy sources in the system. Thus, the energy equation becomes an essential component of the Navier–Stokes equations, particularly in problems where heat transfer, viscous interactions, and phase change processes are significant.

$$\frac{\partial(\rho E)}{\partial t} + \nabla \cdot \left[\vec{V}(\rho E + p) \right] = \nabla \cdot \left[k\nabla T + \left(\tau \cdot \vec{V}\right) \right] + S_E \tag{2.5}$$

The total energy term E used in the energy equation consists of the fluid's internal energy combined with its kinetic energy and expresses how the temperature field evolves with the flow motion. S_E indicates an additional source term, representing the latent heat transfer that occurs during phase change in condensation-evaporation physics.

2.1.2. Species Transport Equations

In the model, air and water vapour are defined as separable species; thus, the system is treated as a multi-component fluid mixture. Consequently, the diffusion transport of vapour, the change in mass fractions with respect to time and location, and the saturation conditions that give cause to phase change can be calculated in detail. No chemical reactions are assumed in the model; only physical transport and diffusion processes are considered [15].

The fundamental transport equation solved for each species within the species transport model is as follows:

$$\frac{\partial(\rho Y_i)}{\partial t} + \nabla \cdot \left(\rho \vec{V} Y_i\right) = -\nabla \cdot \vec{J}_i + S_i \tag{2.6}$$

Where ρ denotes the density of the mixture, Y_i denotes the mass fraction of the relevant species, J_i denotes the diffusion flux of the species, and S_i denotes the external source term (e.g. mass transferred to the film phase due to condensation).

The species transport model considers not only the transport of water vapour but also the dependence of the thermophysical properties of the mixture on species composition. Accordingly, it is assumed that properties such as density, dynamic viscosity, thermal conductivity, and specific heat of the air-water vapour mixture are calculated based on the mass fractions of the species. The properties of the mixture are modelled using the following weight-average expressions:

The density of the mixture:

$$\rho = \rho_{air} + \rho_{vapor} \tag{2.7}$$

The dynamic viscosity of the mixture:

$$\mu = (1 - w_{vapor})\mu_{air} + w_{vapor}\mu_{vapor} \tag{2.8}$$

The specific heat at constant pressure of the mixture:

$$c_p = (1 - w_{vapor})c_{p,air} + w_{vapor}c_{p,vapor} \tag{2.9}$$

The thermal conductivity of the mixture:

$$k = (1 - w_{vapor})k_{air} + w_{vapor}k_{vapor} \tag{2.10}$$

During the numerical calculations, thermophysical properties are treated as constant and using their mean values between the free-stream flow and the wall surface [16, 17].

2.1.3. Eulerian wall film model

In this study, the Eulerian Wall Film (EWF) model in ANSYS Fluent software is used to numerically represent the condensation–evaporation processes occurring on the helicopter windscreen and the resulting fogging–defogging behaviour. When the water vapor obtained by solving the moist-air conditions falls below the dew point on the windshield surface, it causes the formation of a liquid phase; and this film exhibits filmwise characteristics. The EWF model allows for the two-dimensional calculation of the film thickness, the film velocity, and the mass–heat transfer of this thin liquid layer formed on the wall. Thus, the formation, movement, and interaction of the water film on the windshield surface with the air blown onto it can be modelled entirely on a physical basis. This makes it possible to numerically predict defogging performance [15].

The EWF model solves the mass, momentum, and energy conservation equations of the liquid film formed on the surface as a two-dimensional flow along the windshield, enabling the determination of the film thickness, average velocity within the film, and temperature, while also accounting for effects such as shear stresses from the gas phase, pressure gradients, gravity, and surface tension. Even though the model's structure allows for modelling processes such as droplets impinging on the wall and joining the film, splashing, or stripping, only filmwise condensation–evaporation, fluid dynamics along the film, and the shear effect from the air flow were considered in this study, according to the physical problem definition. Thus, the accumulation of the thin film on the helicopter windscreen over time, its movement along the surface, and its drying by the warm air flow are modelled within the basic physical processes required for the defogging phenomenon [15].

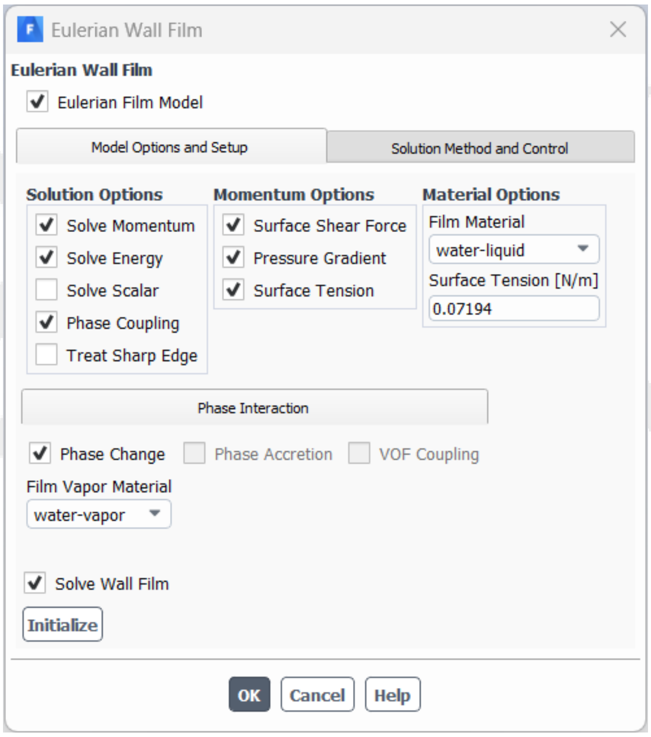

Figure 2. 1 : Eulerian Wall Film model setup screen in Fluent

The wall film settings used in this study are defined by the EWF interface shown in Figure 2. 1. When setting up the model, the physics of windshield defogging are taken into account.

First of all, the conservation of mass for a two dimensional film in a three dimensional domain is [15]:

$$\frac{\partial \rho_l h}{\partial t} = \nabla_s \cdot \left(\rho_l h \vec{V_l}\right) = \dot{m}_s \tag{2.11}$$

where ρ_l is the liquid density, h the film height, ∇_s the surface gradient operator, $\vec{V_l}$ the mean film and $\dot{m}_s$ the mass source per unit wall area due to droplet collection, film separation, film stripping, and phase change. In this study, the mass source parameter consider only due to the phase change.

With the Solve Momentum option, the film flow is modelled as being able to move along the surface due to the shear force applied by both gravity and air flow. The film momentum equation is given as follows [15]:

$$\frac{\partial \rho_l \vec{V_l}}{\partial t} + \nabla_s \cdot \left(\rho_l h \vec{V_l}\vec{V_l} + \overline{\overline{D}}_v\right) = -h\nabla_s P_L + \rho_l h \vec{g}_\tau + \frac{3}{2}\vec{\tau}_{fs} - \frac{3\mu_l}{h}\vec{V_l} + \dot{\vec{q}}_s + \vec{\tau_{\theta_w}} \quad (2.12)$$

where

$$P_L = P_{gas} + P_h + P_\sigma \quad (2.13)$$

$$P_h = -\rho h(\vec{n} \cdot \vec{g}) \quad (2.14)$$

$$P_\sigma = -\sigma \nabla_s \cdot (\nabla_s h) \quad (2.15)$$

The physical equivalents of the terms in these equations are as follows:

Left-Hand Side (LHS): This section represents transient and convection effects.

It employs a tensor $\overline{\overline{D}}_v$ for the differential advection term, calculated assuming the film's velocity profile is quadratic.

Right-Hand Side (RHS): The terms here represent the following physical forces in order:

1. Pressure & Spreading Term: Combines gas-flow pressure, the gravity component normal to the wall and surface tension.
2. Gravity Term: The effect of gravity running parallel to the film.
3. Viscous Shear Term: The third and fourth terms define shear forces at the gas-film and film-wall interfaces (derived assuming a parabolic velocity profile).
4. Droplet Dynamics: Accounts for droplet separation or collection.
5. Surface Forces: Represents effects caused by the contact angle and liquid surface tension.

With the Solve Energy option, the thermal behavior of the film is modeled by accounting for the transient and convective transport of energy within the liquid layer, as well as the heat fluxes and latent heat effects arising from gas–film and film–wall interactions. The film energy equation is given as follows [15]:

$$\frac{\partial \rho_l h T_f}{\partial t} + \nabla_s \cdot \left(\rho_l h T_f \vec{V_l} + \vec{D}_T\right) = \frac{1}{C_p}\left[\frac{2k_f}{h}(T_s + T_w - 2T_m) + \dot{q}_{imp} + \dot{m}_{vap} L\right] \quad (2.16)$$

The physical equivalents of the terms in these equations are as follows:

Left-Hand Side (LHS): This section represents transient and convection effects.

1. Transient term: Indicates the change in the total energy storage in the film over time.
2. Convective term: Represents the energy carried by the film's movement across the surface.
3. Differential advection correction ($\vec{D}_T$): It corrects the effect of the accepted quadratic temperature profile within the film on the average energy.

Right-Hand Side (RHS): The terms here represent the following physical forces in order:

1. Conductive heat flux across interfaces: The net heat flux transferred across the gas–film and film–wall interfaces is represented; this flux depends on the thermal resistance of the film, and heat transfer decreases as the film thickness increases. ($R_f = h/k_f$)
2. Droplet impingement heat source: It represents the heat transferred to the film by liquid droplets hitting the wall; it is disabled in this study.
3. Latent heat term: It refers to the contribution of latent heat released or consumed during condensation or evaporation to the film's energy.

The Solve Scalar option enables the modelling of the transport of additional components or passive scalars that may be present within the film phase under the Eulerian Wall Film model. However, since the liquid film on the wall in this study is considered to be a single-component water film formed by the condensation of water vapour, there is no additional scalar to be tracked within the film, and therefore this option has not been included in the solution [15].

Treat Sharp Edge is not required; the helicopter window does not contain sharp edges that could cause separation or tearing in the wall film [15].

The Phase Coupling option allows condensation and evaporation processes occurring between the liquid and gas phases to be represented consistently in both phases using the Eulerian Wall Film model. In this study, this option is enabled in order to physically accurately model the development of the liquid film formed on the wall surface with its phase change. The film phase is selected as ‘water-liquid’ and the film vapour phase as ‘water-vapor’, assuming that condensation on the windshield occurs only as water condensation [15].

The Surface Shear Force option incorporates the shear stress created by the gas phase flow on the liquid film into the momentum equation. During the defogging process, the air flow blowing across the windshield surface is one of the primary driving mechanisms for the transport and thickening of the liquid film; therefore, this effect is necessary for the accurate modelling of the film flow [15].

The Pressure Gradient option accounts for the effect of the pressure distribution in the main flow field on film motion. Local pressure gradients caused by the flow developing around the windshield geometry can affect the direction and speed of film flow, particularly on inclined surfaces; therefore, this term has been included in the momentum equations. However, under defogging conditions, the film flow is predominantly driven by shear stress, so this effect is expected to be of minor concern [15].

The Surface Tension option represents the capillary forces associated with the surface tension of the liquid film. In the thin film regime, surface tension affects spreading behaviour and local film thickness distribution; however, it plays a more limited role compared to phase change and surface shear effects, which are the main determining mechanisms in defogging problems. Therefore, this term has been included in the model as a secondary but complementary effect [15].

The Phase Accretion option represents the addition of mass to the film phase as a result of discrete liquid droplets in the gas phase impinging on the wall surface. In this study, the liquid film on the windshield surface is formed only by the condensation of water vapour, not by the impact of external droplets. Therefore, it is not consistent with the physical problem definition representing droplet–film interaction. Consequently, the Phase Accretion option is not included in the solution [15].

2.2. Turbulence Modelling

Turbulent flows are characterised by irregular velocity fluctuations that depend on time and space. These fluctuations occur within interactions spanning a very wide range of length and time scales. This situation results in momentum and energy transfer mechanisms having a highly complex structure, making it difficult to define turbulence analytically in its entirety. For this reason, turbulence modelling presents a fundamental and critical problem in computational fluid dynamics studies.

Numerically, turbulence flows can be solved most accurately using the direct numerical simulation (DNS) method. In the DNS approach, the Navier–Stokes equations are solved without the need for any turbulence model, and all scales of turbulence are calculated directly. Although this method theoretically produces accurate results, the computational cost increases very rapidly and becomes impractical for real engineering problems. In the large-eddy simulation (LES) method, developed as an alternative to DNS, large-scale turbulent structures are solved, while small-scale eddies are modelled. Although LES offers higher accuracy compared to RANS methods, it requires high mesh resolution and small time steps, particularly in regions close to walls, resulting in a very high computational cost. For these reasons, both DNS and LES methods are not suitable for routine use in engineering applications with complex geometries and dominant wall effects [15, 18].

The primary objective of this study is to investigate the behaviour of air flow and the transport mechanisms associated with the wall surface under demisting conditions. In the physical problem under investigation, the flow characteristics are largely determined by momentum, heat, and mass transfer near the wall, and it is not necessary to solve large-scale time-dependent turbulence structures in detail. Accordingly, considering the balance between solution accuracy and computational cost, it is considered appropriate to use a time-averaged turbulence modelling approach. Within this scope, the Reynolds-Averaged Navier–Stokes (RANS) approach has been preferred in the demisting CFD analyses. In the RANS method, flow variables are separated into their mean and turbulent components, and only the mean flow field is numerically solved. When applying RANS modelling, different turbulence models can be used, taking into account the flow regime, wall effects, and possible flow separations. In general, RANS-based turbulence models are classified into three main categorizes consisting of Spalart–Allmaras, k–ε, and k–ω based models.

In Reynolds averaging, each variable in the instantaneous Navier–Stokes equations is split into a mean part and a fluctuating part. In particular, the velocity components are expressed as the sum of their time-averaged values and the corresponding turbulent fluctuations [15, 18]:

$$u_i = \bar{u}_i + \acute{u}_i \tag{2.17}$$

where $\bar{u}_i$ and $\acute{u}_i$ are the mean and fluctuating velocity components.

The Reynolds-averaged Navier–Stokes momentum equations written in terms of average velocities are obtained as follows:

$$\rho\left(\frac{\partial \bar{u}_i}{\partial t} + \bar{u}_j \frac{\partial \bar{u}_i}{\partial x_j}\right) = -\frac{\partial \bar{p}}{\partial x_i} + \mu \frac{\partial^2 u}{\partial x_j^2} - \frac{\partial}{\partial x_j}\left(\rho \overline{u_i' u_j'}\right) \tag{2.18}$$

The $-\rho\overline{u_i' u_j'}$ term in this equation is referred to as Reynolds stresses, representing the effect of turbulent velocity fluctuations on the mean flow. Using the eddy viscosity assumption, Reynolds stresses are modelled as follows:

$$-\rho\overline{u_i' u_j'} = \mu_t\left(\frac{\partial \bar{u}_i}{\partial x_j} + \frac{\partial \bar{u}_j}{\partial x_i}\right) - \frac{2}{3}\rho k S_{ij} \tag{2.19}$$

Where μ_t denotes turbulence viscosity and k denotes turbulence kinetic energy. The fundamental difference between the Spalart–Allmaras, k–ε, and k–ω turbulence models comes from the way of calculating turbulence viscosity [15, 18].

2.2.1. Spalart-allmaras model

The Spalart–Allmaras turbulence model is a RANS turbulence model based on the eddy viscosity assumption and solving a singular transport equation. Although developed for external aerodynamic applications, the model is widely used in many engineering problems due to its low computational cost and numerical stability.

In the Spalart–Allmaras model, instead of directly calculating μ_t, the transport equation is solved for an auxiliary variable ($\tilde{\nu}$) related to turbulent viscosity. Using this variable, turbulent viscosity is defined as follows:

$$\mu_t = \rho \tilde{\nu} f_{\nu 1} \tag{2.20}$$

Here, ρ refers to fluid density, $\tilde{\nu}$ indicates the Spalart–Allmaras model-specific turbulence viscosity variable, and $f_{\nu 1}$ signifies the model function that accounts for viscous damping effects. Thus, Reynolds stresses are closed using a singular turbulence transport equation.

The most significant advantage of the Spalart–Allmaras model is that it offers lower computational costs compared to RANS models with the other two equations. However, the model may exhibit limited accuracy in problems where strong flow separations, complex vortex structures, and heat and mass transfer near walls. [15, 18].

2.2.2. k- ε model

The k–ε turbulence model is a RANS turbulence model based on the eddy viscosity assumption and solving two transport equations. In the model, the turbulent flow field is defined using the variables turbulent kinetic energy (k) and turbulent dissipation rate (ε). In the k–ε model, the turbulent viscosity is calculated using the k and ε values as follows:

$$\mu_t = C_\mu \rho \frac{k^2}{\varepsilon} \tag{2.21}$$

Here, it refers to the C_μ model constant.

The standard k–ε model provides successful results in free-stream regions and fully developed turbulent flows; however, it may exhibit limited accuracy in flows near walls and regions with negative pressure gradients. In addition to the standard k–ε model, two different variants have been developed in the literature: RNG k–ε and Realizable k–ε. The RNG k–ε model can provide better results than the standard model, particularly in flows with high velocity gradients. The Realizable k–ε model aims to solve flow separations and rotational flows more realistically through improvements in the definition of turbulence viscosity and the formulation of the ε equation. However, the solution accuracy in flows near walls may remain limited in all three k–ε variants.

2.2.3. k- ω model

The k–ω turbulence model is a RANS turbulence model based on the eddy viscosity assumption, which solves two transport equations for turbulence kinetic energy (k) and specific dissipation rate (ω). The model has been developed specifically to aim for a more accurate representation of flows near walls. In the k- ω model, the turbulence viscosity is defined as follows:

$$\mu_t = \rho \frac{k}{\omega} \tag{2.22}$$

This formulation allows for the calculation of turbulence viscosity directly based on the flow behaviour near the wall, thereby reducing dependence on additional wall functions. This feature makes the k–ω model advantageous for boundary layer problems where wall effects are dominant. In the standard k–ω model, the turbulence levels defined in free steam flow can significantly affect the solution results. Therefore, the k–ω SST (Shear Stress Transport) model, an enhanced form of the standard k–ω model, is widely used in the literature. In the SST approach, the k–ω model is used near the wall, whereas k–ε is dominant in free-stream regions, thus combining both models' strengths. Furthermore, the SST model enables more accurate prediction of negative pressure gradients and flow separations.

Moreover, in thermal problems, the accuracy of the solution largely depends on the correct estimation of velocity and temperature gradients near the wall. Since the convective heat transfer coefficient is directly determined by these gradients, the performance of the turbulence model within the boundary layer is vitally important. In this respect, the k–ω SST model provides reliable results in both hydrodynamic and thermal problems due to its high resolution near the wall and is widely preferred in the literature [15, 18].

2.2.4. Selection of the turbulence model

In this study, the condensation problem occurs directly on the wall surface; therefore, accurately representing the flow around the wall is critically important. The velocity and shear stresses near the wall are important factors in the condensation process, and the accuracy of the solution in these regions directly affects the numerical results.

In addition, the solution to the problem also involves heat transfer, so the turbulence model must be able to reliably predict the velocity and temperature gradients within the boundary layer. In such thermal problems, turbulence models that can directly solve the flow near at the wall and reduce the dependence on additional wall functions offer a more suitable approach.

In this regard, among the evaluated RANS-based turbulence models, the k–ω SST model is determined to be the most suitable option because it can represent the flow within the boundary layer with high accuracy by using the k–ω formulation near at the wall and increase solution stability by exhibiting k–ε solution in free-stream regions. Furthermore, the validation results presented in the following sections of the study confirm the suitability of the selected turbulence model for the current problem and the reliability of the solution [15, 18].

2.3. Near Wall Treatment and Boundary Layer Resolution

The wall condensation phenomenon, which is the subject of this study, occurs directly on the wall surface as a result of the interaction between the fluid and the solid surface. Wall condensation is a complex process involving the combined effects of momentum, heat, and mass transfer. In particular, the gradients of velocity, temperature, and species components formed in regions near the wall surface during condensation directly determine condensed liquid quantity and the behaviour of the formed liquid film. In this respect, accurate modelling of the flow field near the wall is critical for the reliable prediction of the condensation process, which involves both heat transfer and phase change.

The numerical modelling approaches used for flow near walls are generally referred to as near-wall treatment. In turbulent flows, it is possible to directly solve regions where viscous effects are dominant within the boundary layer or to model them using wall functions. However, wall function-based approaches are generally based on empirical assumptions and offer limited accuracy in modelling sensitive processes such as condensation and heat transfer occurring on the wall surface. In this study, since the nature of the condensation phenomenon requires detailed resolution of the physical processes near the wall, a near-wall approach that directly solves the wall instead of wall functions is preferred.

The turbulent flow structure near the wall is characterised by the parameter y+, defined as the dimensionless wall distance. The boundary layer consists of different sublayers: the viscous sublayer closest to the wall surface, the buffer layer above it, and the log-law (fully turbulent) region further away. The velocity profiles and physical behaviour of these layers differ from one another. As shown in Figure 2.2, the dimensionless u+ velocity profile in the viscous sublayer region exhibits an approximately equal relationship with the y+, and viscous effects are dominant in this region. The buffer layer immediately above this region represents the transition zone where viscous and turbulent effects are both effective, while turbulent flow behaviour becomes dominant in the log-law region.

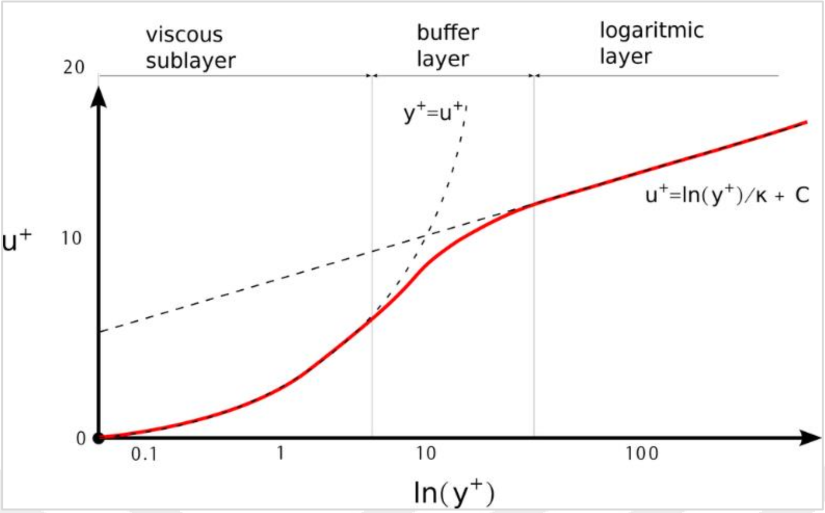

Figure 2. 2 : Turbulent boundary layer

In heat transfer problems, particularly those involving wall condensation, temperature and species component gradients reach their highest values within the viscous sublayer. Therefore, the cell nearest to the wall surface must be positioned so that it can directly resolve this region. Considering the boundary layer structure given in Figure 2. 2, it can be seen that for this condition to be satisfied, the dimensionless wall distance must be y+<1. This approach allows the velocity and temperature profiles within the boundary layer to be solved numerically without approximation and enables more realistic modelling of the heat and mass transfer mechanisms associated with condensation.

The k–ω SST turbulence model used in this study is based on the k–ω formulation near the wall and can represent the flow within the boundary layer with high accuracy and is suitable for use with low y+ values. Accordingly, the mesh structure is created to ensure y+<1 in the cells closest to the wall surface, providing sufficient resolution throughout the boundary layer. Thus, both the turbulent flow behaviour near the wall and the condensation and heat transfer processes are modelled in a physically realistic way [19].

2.4. CFD Solution Methodology

In this section, the methods used to numerically solve the physical and mathematical model defined in the previous sections are presented. The discretisation approaches applied during the solution process, solver settings, mesh structure, and issues related to numerical stability are fundamental elements that directly affect solution accuracy and computational efficiency. In this context, the numerical methods and solution parameters used are systematically addressed under subheadings.

2.4.1. Spatial and temporal discretization

The flow, heat transfer, and mass transfer equations defined in this study are discretized using the finite volume method with the commercial CFD software ANSYS Fluent 24R1. The governing equations are integrated over control volumes to form algebraic equations and solved numerically. This approach provides a reliable solution framework in terms of mass, momentum, and energy conservation for problems with complex geometries.

Within the spatial discretization scheme, a second-order upwind scheme is used for all equations of momentum, energy, turbulence, and species transport. Second-order discretisation schemes improve solution accuracy compared to first-order approaches, enabling a more realistic representation of physical field changes.

Since condensation and fogging occur over time, the temporal variation of the flow field constitutes an essential part of the solution. The fog film forming on the windshield surface is modelled by solving its governing equations defined within the Eulerian Wall Film (EWF) model. Therefore, the time-dependent evolution of the fog film is solved using a transient approach. In contrast, a steady-state solution is preferred for the flow field. The main reason for this is that, as will be presented in subsequent sections, a comparison of the flow solved in steady and transient states yields similar flow characteristics. Solving the flow field in steady state allows for significant savings in computation time (CPU time-hour) without compromising solution accuracy.

2.4.2. Solver settings

A coupled solution algorithm is preferred for the pressure-velocity coupling. In this approach, the continuity and momentum equations are solved simultaneously to enhance solution stability. Also, second-order interpolation scheme is used for the discretization of the pressure field. The convergence criterion for the solution is based on the residual values for all governing equations falling below the 10^{-5} level.

2.4.3. Mesh strategy

The computational domain is discretized through a mesh structure formed by polyhedral cells. When defining the mesh structure, mesh independence and first layer thickness independence studies are performed to prevent numerical errors that may occur due to the inter-cell connection structure. As a result of these studies, the most suitable mesh structure representing solution accuracy is determined.

To accurately represent the flow and condensation process near the wall, the mesh structure is created in accordance with the near-wall solution. In this scope, special attention is paid to adjusting the size of the cells closest to the wall surfaces so that the dimensionless wall distance $y^+<1$. Thus, the velocity, temperature, and species gradients within the boundary layer are solved directly, yielding a numerical solution consistent with the k–ω SST turbulence model used.

3. NUMERICAL VALIDATION OF THE WALL CONDENSATİON MODELLING

Wall condensation is a highly complex heat–mass transfer problem which involves the coupled effects of phase change, multi-component mass diffusion, convective heat transfer, and turbulence interactions. In order to reliably model this kind of physics in a numerical environment, the used methodology must be verified with experimental data to ensure that it correctly simulates the main condensation mechanisms. For this purpose, the CONAN experimental setup, developed by Ambrosini et al. (2008) at the Pisa University and accepted as a reference in the literature, is used as a comprehensive validation setup. In this section, the validity of the model is discussed by comparing the data obtained in the experimental study with numerical analyses conducted under the same conditions. In this way, the reliability of the numerical approach based on wall condensation physics is demonstrated, and a methodology is developed that can be applied to different engineering applications in the following sections.

3.1. Description of the CONAN Facility Experimental Setup

The CONAN test set-up, developed to enable the investigation of wall condensation processes under controlled laboratory conditions, is a reference experimental platform widely used in the literature [8, 20]. As wall condensation is a complex process, the highly accurate experimental data provided by this apparatus is internationally accepted as the standard for evaluating the validity of numerical models.

The experimental setup is made up of two flow channels in conjugate heat transfer configuration, separated by a 45 mm thick aluminium plate. The primary channel side of the plate is in contact with moist air flowing downwards. This air-water vapour mixture, which hits the plate surface cooled below the dew point, condenses on the surface and passes into the liquid phase; the resulting liquid layer flows downwards under the gravity influence and collects at the channel outlet. The opposite side of the plate is in contact with cold water flowing through the secondary channel, creating the necessary thermal difference for condensation. The primary channel has a square cross-section with a length of 0.34 m. Three honeycomb flow regulators placed at the channel inlet regulate the flow velocity profile, increasing the repeatability of the experimental conditions. The secondary channel is 5 mm deep and allows heat to be extracted from the plate by the upward flow of cold water. The opposite directions of the two flows create a marked temperature gradient within the plate, providing the thermodynamic effect necessary for condensation. The schematic sketch of the CONAN facility test setup is shown in Figure 3. 1.

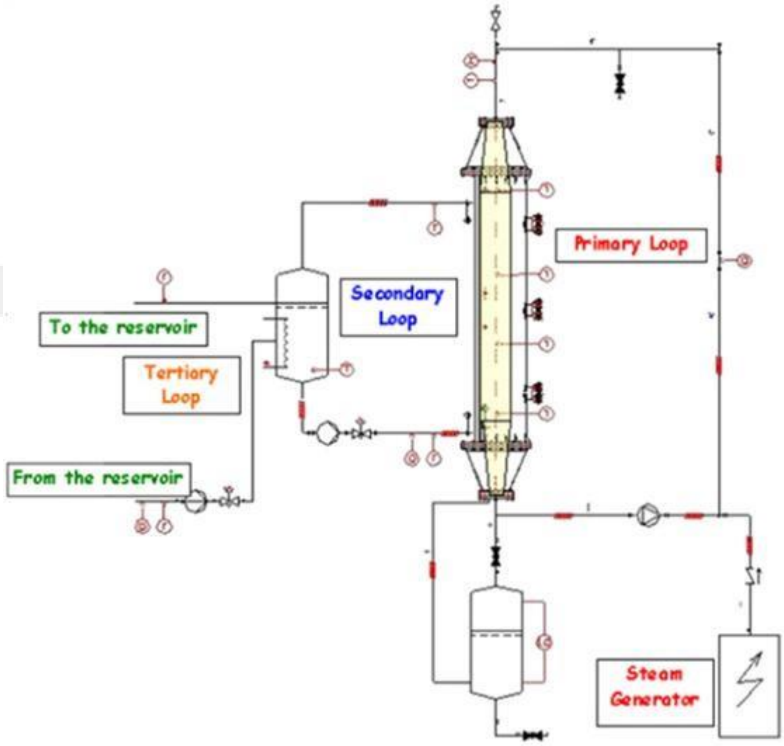

Figure 3. 1 : Sketch of the CONAN Facility [20]

K-type thermocouples were used to determine the temperature and surface heat flux within the plate at different depths. The measurement accuracy of these thermocouples is typically within a range of ±0.25°C, and systematic errors were minimised by calibrating them prior to the experiment. The positioning of the thermocouples allows both the temperature distribution within the plate and the wall heat flux to be obtained. The heat flux accuracy derived from the thermocouple data is ±700W/m². The condensing liquid flow rate was collected in a collection unit at the bottom surface of the plate, and the flow velocity was continuously monitored using a high-precision differential pressure transducer. This transducer is capable of providing reliable readings even at low flow rates. Thus, the condensation flow rate, which varies over time, was measured with a tolerance of less than 1%, and reliable reference data was provided for comparison with the numerical model.

3.2. Geometrical Definitions and Boundary Conditions of the Test Bench

In the test setup at the facility, there is a 45mm thick aluminum plate between two channels. The primary channel where the condensation process takes place has a square cross section and is 0.34m in length on each side. The secondary channel, which contacts the rear side of the aluminum plate and performs heat transfer through the primary channel via the plate, is 5mm deep and 0.34m wide. In the 2m long system, the primary channel flows from upstream to downstream while the secondary channel flows from downstream to upstream. Upstream have three honeycomb panels (35 mm thick, 3mm cell diameter) ensure a uniform inlet velocity distribution, while lateral channel sides are considered adiabatic. All the dimensions that mentioned above are shown in Figure 3. 2.

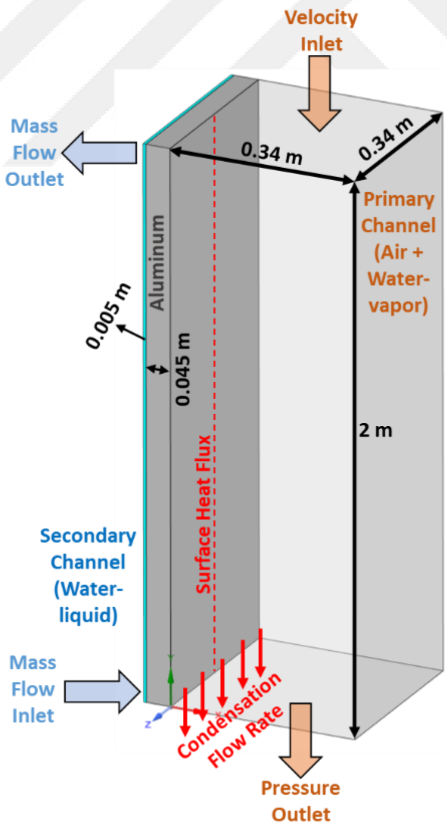

Figure 3. 2 : Numerical modelling of the CONAN Test Bench

There is a crossflow regime with the primary and secondary channels in the CONAN test setup as shown in Figure 3.2. The atmospheric air that contains air with water-vapor flows from the primary channel and the water-liquid flows from the secondary channel. There were many test cases performed in the CONAN facility. The flow parameters of the five tests carried out at the CONAN facility are given in Table 3. 1.

Table 3. 1 : Boundary conditions of the CONAN test setup [8]

Case No	Test No	Primary Cannel (Air + Water-vapor)			Secondary Channel (Water-liquid)	
		$V_{in,Mix}$ [m/s]	$RH_{in,Mix}$ [%]	$T_{in,Mix}$ [°C]	$T_{in,water}$ [°C]	$V_{in,water}$ [m/s]
1	P10 – T30 – V15	1.46	100	82.66	31.24	1.217080
2	P10 – T30 – V20	2.02	100	80.61	31.10	1.217269
3	P10 – T30 – V25	2.52	97.83	79.13	31.07	1.216775
4	P10 – T30 – V30	3.01	87.35	78.73	30.91	1.216021
5	P10 – T30 – V35	3.59	96.55	75.02	30.91	1.215940

3.3. Mesh Generation and Grid-Independence Study

The selection of the mesh structure used in the numerical solution has a decisive impact on both computational accuracy and solution cost. Accordingly, a mesh structure consisting of polyhedral cells that provide a homogeneous solution in flow regions and apply sensitive layering near walls has been preferred in three-dimensional structures, balancing accuracy and computational cost. The boundary layer region where condensation intensifies on surfaces in contact with the plate is an area where flow characteristics change rapidly. Therefore, a boundary layer structure is employed in these areas in the direction of the wall normal. To ensure that the turbulence model accurately captures wall effects, the target criterion $y^+ < 1$ was taken into account, and the initial cell height was determined accordingly. This allows both the location of the condensation interface and the behaviour of the wall sublayer to be resolved in more physical terms.

Two different mesh types are used to determine appropriate types. These are hexahedral structured mesh and polyhedral mesh as shown in Figure 3. 3. The effects of these meshes with the same boundary layer are examined on the condensate flow rate results. The results showed that there is no dramatic change between hexahedral and polyhedral mesh, but the mesh cell number of polyhedral mesh is much less than hexahedral mesh. Polyhedral mesh method is preferred for future work because of the computational cost.

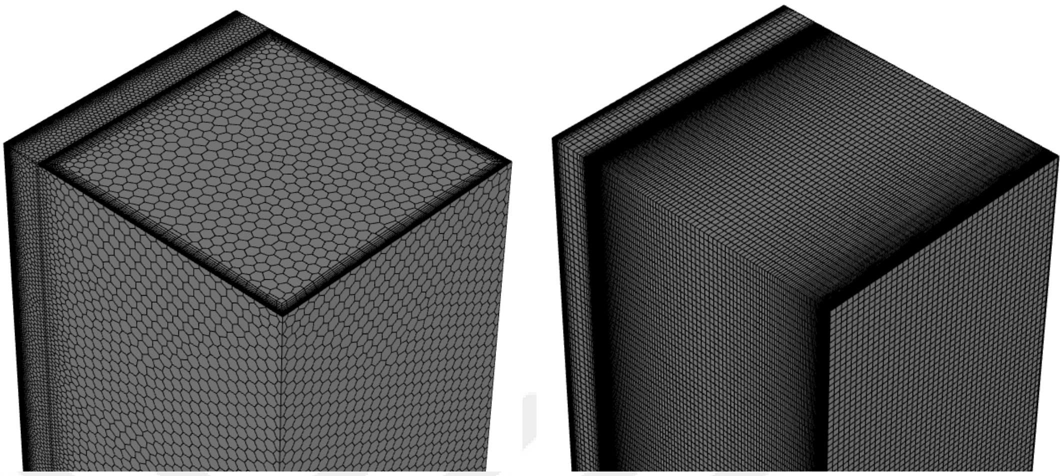

(a) Polyhedral Mesh (b) Hexahedral Mesh

Figure 3. 3 : Different mesh types

In order to prevent numerical results from being affected by grid intensity, a grid independence study is conducted. While performing mesh independence, the boundary layer parameters are kept constant and the mesh sizing between analyses is performed with a 1.33 factor. Figure 3. 4 presents the condensation mass flow rate results of the P10-T30-V15 obtained from CFD simulations for five different mesh intensities, labeled as Analysis 1 through Analysis 5. For comparison, the experimental result is also plotted as a dashed red line, with a value of 2.3 g/s.

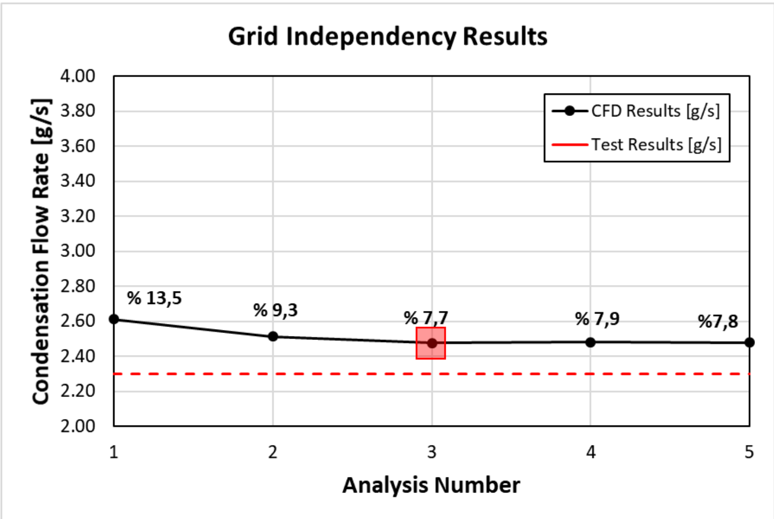

Figure 3. 4 : Grid independency results

As shown in the Figure 3. 4, in the coarsest mesh (Analysis 1), there is a deviation of 13.5% from the experimental result and, with increasing mesh number, the deviation decreases significantly. From Analysis 3 onward, the predicted values converge, with only marginal differences observed between Analyses 3, 4, and 5 (7.7%, 7.9%, and 7.8% deviation, respectively). This indicates that further mesh refinement has a negligible effect on the simulation results. Therefore, Analysis 3 is selected as the optimal mesh configuration for the remainder of the simulations.

However, although the grid independence study has converged, still important is to mention that the condensation phenomenon occurs dominantly on the wall surfaces. Consequently, the independence of the boundary layer has a more pronounced effect on the accuracy of CFD predictions. Therefore, an additional sensitivity analysis focusing on the first layer thickness has been performed while keeping the total boundary layer thickness constant. This approach ensures adequate resolution of near-wall gradients, particularly in regions where phase change and heat transfer are dominant. Table 3. 2 summarizes the boundary layer parameters employed in the first layer thickness independence study conducted with nine different boundary layer configurations. The mesh sizes used in these meshes are based on the results obtained from mesh independence.

Table 3. 2 : Boundary layer parameters of FLT independent study

Analysis Number	First Layer Thickness [mm]	Layer Number	CFD Results [g/s]
1	No Boundary Layer		2.81
2	5.04	3	2.41
3	2.52	5	2.03
4	1.26	7	1.70
5	0.63	10	1.48
6	0.32	14	1.49
7	0.16	17	1.50
8	0.08	21	1.51
9	0.04	24	1.52

Figure 3. 5 illustrates the results of the first layer thickness independency analysis for case P10-T30-V15. Similar to the grid independence study, the condensation mass flow rate results calculated by CFD simulations are compared with the experimental

result of 2.3 g/s. As seen in the figure, for large first layer thicknesses (Analyses 1–3), the deviation from the experimental value is significantly high (56.1%, 38.8%, and 22.1%, respectively). However, as the first layer thickness is refined, the results converged toward to the experimental measurement. From Analysis 5 onward, the difference between successive simulations became negligible (1.7%, 1.2%, 0.7%, 0.4%, and 0.1%). This indicates that the near-wall resolution has a dominant influence on the condensation prediction accuracy compared to overall grid refinement.

Consequently, Analysis 5 is selected as the optimum configuration after grid and first layer thickness independent studies, ensuring both numerical accuracy and computational efficiency. With this setup, sufficient near-wall resolution is achieved while more accurate results avoiding unnecessary computational cost associated with further refinement.

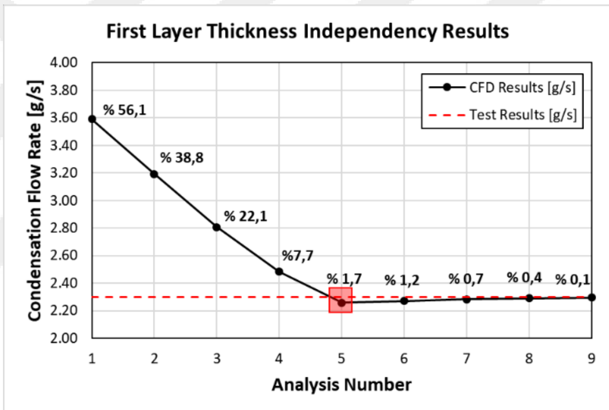

Figure 3. 5 : First layer thickness independency results

3.4. Comparison of Numerical Results with Experimental Measurements

Following mesh independence and modelling steps, numerical analyses are performed for five different operating conditions reported at the CONAN facility, and the results obtained are compared with experimental measurements. For the comparison, two quantities are evaluated. One quantity is the local surface heat flux obtained at the centre line along the primary channel side of the aluminium plate, and the other quantitiy is the mass flow rate of condensation measured at the primary channel outlet. These two quantities are indicators of both heat transfer and mass transfer in wall condensation physics.

Figure 3. 6 presents a comparison of surface heat flux between CFD solutions and experimental measurements. According to common applications in the literature, a

10% error margin in local heat flux results is considered an acceptable performance limit. When the numerical results are examined, the trend of heat flux variation along the flow direction has been successfully reproduced by CFD. The numerical results remaining within the specified error limits at six of the eight measurement points demonstrate that the model consistently captures the heat transfer behaviour near the surface.

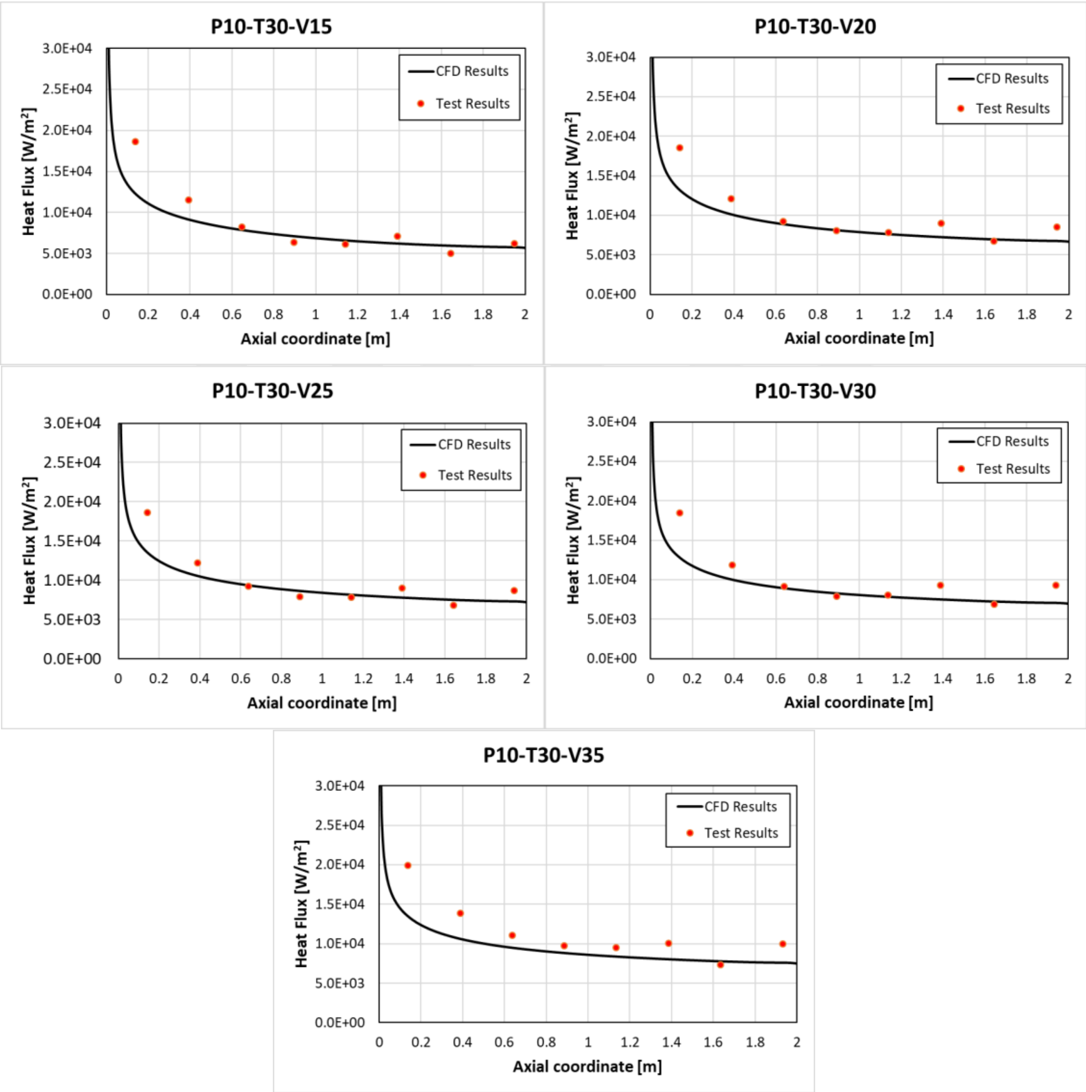

Figure 3. 6 : Surface heat flux comparison of CFD and test results

The deviations at the first two points near the inlet region are related to the flow not being fully developed in this region and the experimental parameters for inlet turbulence not being fully obtained. It is expected that small uncertainties will occur at the inlet level due to parameters such as turbulence intensity and viscosity ratio. Despite these limited deviations, the overall trend is correctly calculated and the physical behaviour of heat transfer along the plate is obtained, confirming the heat transfer accuracy of the model.

The second fundamental criterion in evaluating model accuracy is the condensation mass flow rate measured at the primary channel outlet. Figure 3. 7a compares experimental and numerical flow rates of condensation for each of the five cases, while Figure 3. 7b presents the error rates within a margin of ±10% of the CFD results relative to the experimental values.

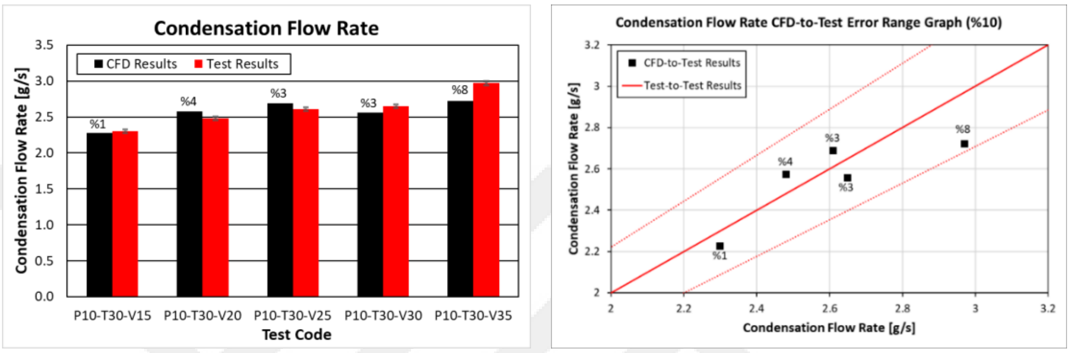

a. Condensation flow rate results b. Error Margin Chart

Figure 3. 7 : Condensation flow rate comparison of CFD and test results

The obtained results demonstrate that the numerical model can calculate the condensation flow rate with high accuracy. Under all operating conditions, the deviation of the CFD results from the experimental measurements remained within the range of 1% to 8%, which is well below the 10% error limit accepted in the literature. This accuracy shows that the phase change and transport mechanisms representing the physics of wall condensation are correctly captured by the numerical solution.

Performance of the CFD approach in accurately representing condensation physics is confirmed by the close agreement of both the surface heat flux distribution and the mass flow rate of condensation with experimental data. While minor deviations exist due to the flow not being fully developed in the inlet region, these differences are not significant enough to affect the accuracy of the wall condensation model. When all analyses are considered together, it is shown that the used numerical methodology can successfully modelling heat and mass transfer behaviour. These validation results indicate that the validation methodology can be reliably used in the helicopter demisting analyses which will be presented in the following sections.

4. NUMERICAL INVESTIGATION OF HELICOPTER DEMISTING PERFORMANCE

In this section, the defogging performance of the helicopter windscreen is examined at different operating conditions by using the numerical model validated in the previous sections. After validating the wall film condensation model, the validated model is transferred to helicopter level and the time-dependent development of the condensation film accumulating on the windscreen surface is evaluated based on airflow and thermodynamic parameters. To ensure the reliability of numerical results, some independence studies are conducted in terms of network structure, first layer thickness, time step, and solution approach. Subsequently, a parametric study and regression analysis are performed to determine the effects of inlet air temperature, humidity, and air flow rate on the total film mass. Finally, based on the regression results for working conditions, the demisting performance for critical view areas is evaluated based on the time-dependent opening behaviour and analysed according to the determined visible value for film thickness.

4.1. Computational Model Description

A simplified numerical model is developed to investigate the defogging performance of a helicopter cockpit windshield. To reduce computational cost and increase solution efficiency, a half model is solved by using the symmetry approach of the helicopter geometry. It is assumed that this method has a negligible effect on flow and condensation characteristics.

The simplified geometry used in numerical analyses is shown in Figure 4. 1. The calculation area consists of the cabin interior, windshield assembly, flight control consol, pilot, pilot seat, ventilation blowers that provide air intake, and a rear channel that provides air outlet. The number of meshes has been reduced by disregarding minor features that are not expected to affect numerical results, such as buttons, crew, instrument tabs, and other trim parts.

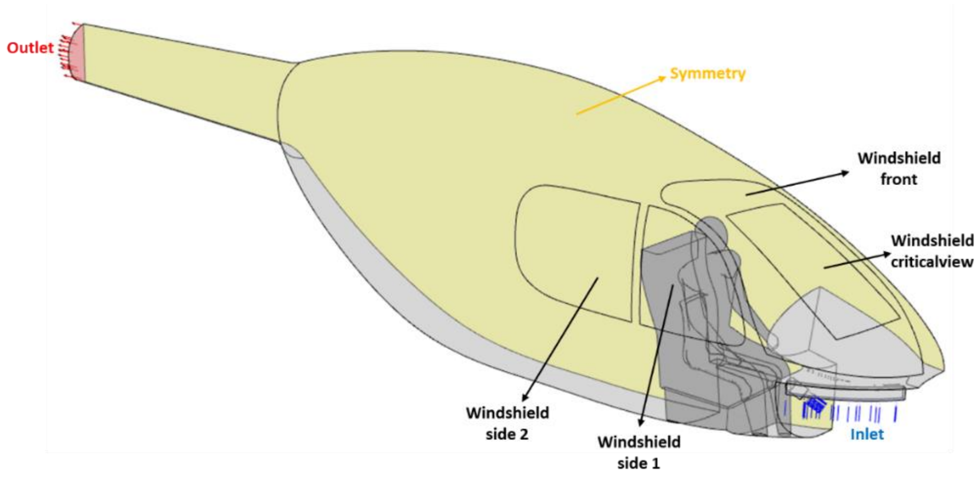

Figure 4. 1 : Simplified geometry of the helicopter analyses

The windshield is consist of three sections. These are the front windshield and two side panels called Side 1 and Side 2. Additionally, the windshield is referred to as two sections due to the defined critical view area. These nomenclature are shown in Figure 4. 2.

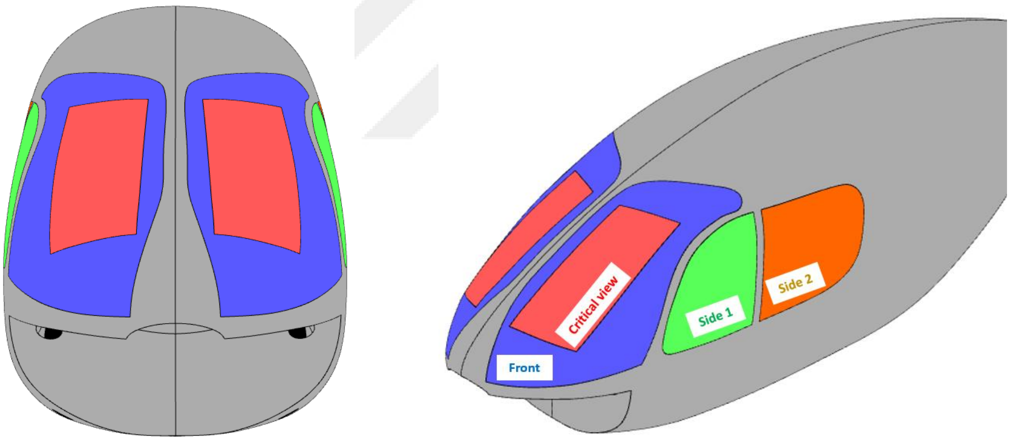

Figure 4. 2 : Windshield nomenclature

4.2. Boundary Conditions and Operating Scenarios

The boundary conditions in the numerical model are defined to represent the operating conditions. Conditioned air entered the cabin through the ventilation blower from environmental control system located on the console at the base of the windshield. These blowers are modeled directed toward the windshield to facilitate removal of the fog film on the windshield; boundary conditions are defined in terms of mass flow rate, specific temperature and mass fraction consistent with scenario definitions. Cabin air is discharged from the rear outlet located in the cut-out of the tail section, which has a gauge pressure of 0 Pa. The ambient air have a 5°C temperature and %90 relative humidity, with water vapor mass fraction of 0.0048. The initial conditions in the analyses are defined according to the environmental conditions inside the cabin so that all working scenarios can be compared. Through this approach, the effects of different parameter combinations on the demisting performance are evaluated based on a joint reference condition, improving the consistency of the regression analysis. The air temperature and humidity in the calculation domain are uniformly assigned at the initial state. On the windscreen surface, the initial condition of the film thickness is defined as 10 μm over the entire windscreen surface. Also, the effect of gravity is taken into account in the analyses. The analyses are evaluated at 5,000 feet and 10,000 feet altitude conditions.

All wall surfaces are modeled as no-slip convection boundary conditions. The convective heat transfer coefficient defined on the windshield surface is determined using various correlations commonly used in the literature to represent the external flow conditions of the helicopter. In this respect, classical correlations proposed for forced convection on a flat plate [1], empirical relationships developed for external flows around elliptical geometries [21], and documented correlations used in military applications are evaluated together. Each correlation is calculated using Reynolds numbers corresponding to a typical helicopter cruise speed. It is observed that the calculated heat transfer coefficients are of similar order across different correlations, and the average of these values is taken to define a constant heat transfer coefficient value. As a result of the evaluations, 50 W/m^2K is selected as a representative value for the examined altitude and speed ranges. This approach ensures a consistent thermal boundary condition across different operating scenarios and allows for a clearer comparison of parameter effects in regression analyses.

4.3. Numerical Independence Studies

This section presents some independence studies aimed at demonstrating that the numerical analyses performed are independent of the mesh structure, time resolution, and solution approach. Within this scope, the sensitivity of the solution results to the selected numerical parameters is systematically examined, and the final numerical setup is determined based on the findings. The independence studies are carried out under four main headings: mesh size, initial film thickness, time step, and solution approach (steady-state/transient). In the evaluations, the total film mass on the front windshield surface and the time-dependent development of the film thickness are used as the basic comparison criteria.

4.3.1. Mesh independence study

It is very important to show that the results obtained in numerical analyses are independent of the selected mesh structure in terms of solution reliability. In this study, which focuses on condensation and film development, a mesh independence study is conducted to evaluate the effect of mesh size on the results.

The number of cells for the six different mesh structures created within this scope are presented in Figure 4. 3. The different mesh structures used in this study are created by increasing the number of cells by a factor of 1.33 compared to the previous mesh level. Analyses conducted under the same boundary and initial conditions showed that there is no significant change in the results after Mesh 4 when basic outputs such as film mass (mass transfer) and heat flux (heat transfer) are examined. While the computational cost increases significantly in finer meshes, the resulting gains remain limited. Therefore, considering the intensive CPU time requirement in regression analyses, the Mesh 4 is selected as the final mesh structure.

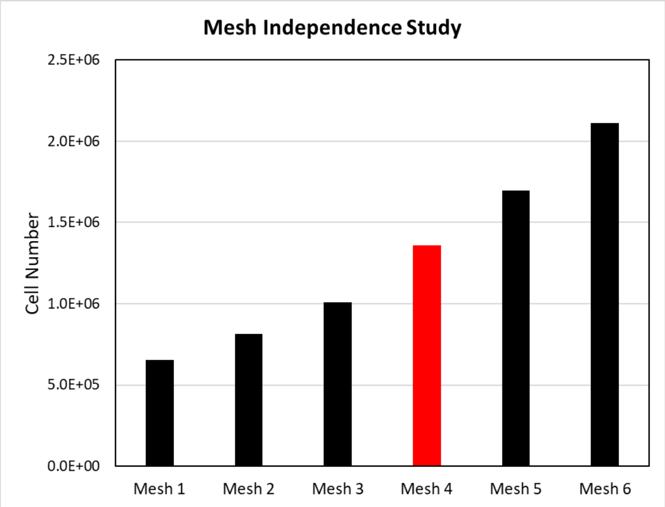

Figure 4. 3 : Cell number of the mesh independence study

The cell distributions for the coarsest mesh, the finest mesh, and the selected Mesh 4 are shown together in Figure 4. 4. It can be seen that the coarsest mesh has limited resolution, particularly in the windscreen and entrance areas, while the finest mesh has a significantly increased cell number. The Mesh 4 mesh is observed to provide sufficient resolution in critical areas while maintaining a balanced structure in terms of computational cost.

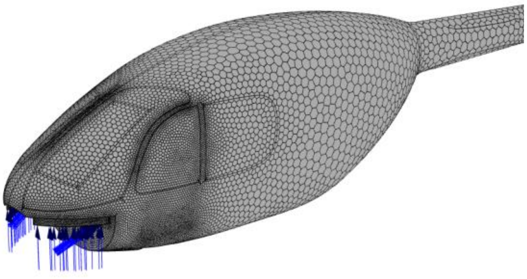

Mesh 1 [Coarsest mesh]

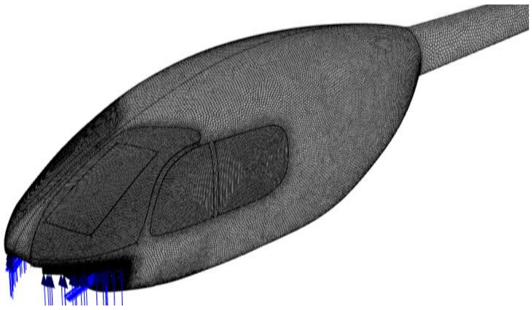

Mesh 6 [Finest mesh]

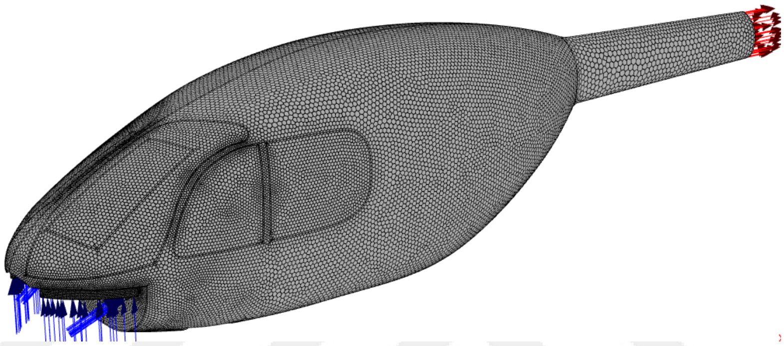

Mesh 4 (Selected mesh)

Figure 4. 4 : Mesh structures of mesh independence study

The time-dependent change in film mass on the windscreen for different mesh structures is shown in Figure 4. 5. When examining the time-dependent film mass curves, it is observed that the film mass decreases over time for all mesh structures and that the demisting process exhibits a similar trend. However, it is noticed that the absolute values of the film mass over time differ slightly depending on the mesh structure. In order to evaluate these differences in more detail, the film mass comparisons at 30 and 60 seconds are examined. These comparisons reveal that there are more significant changes in film mass values between Mesh 1 and Mesh 3, whereas the film mass values calculated for Mesh 4 and finer meshes are quite close to each other. Particularly after Mesh 4, no significant change in the film mass values obtained for both the windscreen and the critical viewing area is observed. These results demonstrate that the Mesh 4 mesh adequately represents the time-dependent development of the film mass with sufficient accuracy and that mesh independence is achieved at this level.

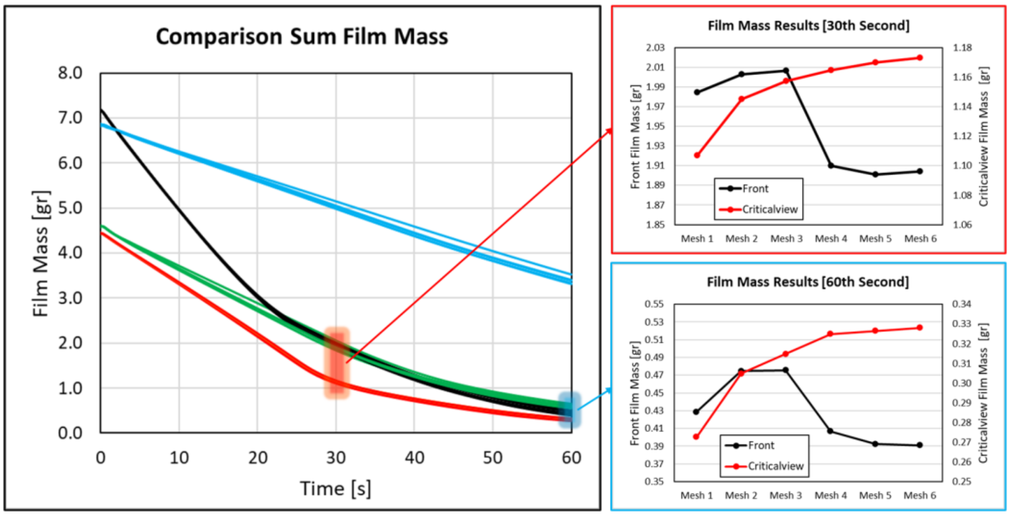

Figure 4. 5 : Film mass results of mesh independence study

The Figure 4. 6 presents the time-dependent change in the average heat flux on the windscreen surface for different mesh structures. Similar to the film mass results, the time-dependent development of the heat flux exhibits the same trend for all mesh structures, but shows limited differences depending on the mesh density. Upon examining the heat flux values at 30 and 60 seconds, provided for more detailed comparisons, it is observed that the results obtained for Mesh 4 and finer meshes are quite close to each other. This indicates that the solution becomes independent of the mesh from the Mesh 4 level onwards, not only in terms of film mass but also in terms of thermal quantities. Accordingly, the Mesh 4 mesh, which represents both condensation and heat transfer results with sufficient accuracy and offers a balanced structure in terms of computational cost, is preferred as the final mesh structure in all analyses.

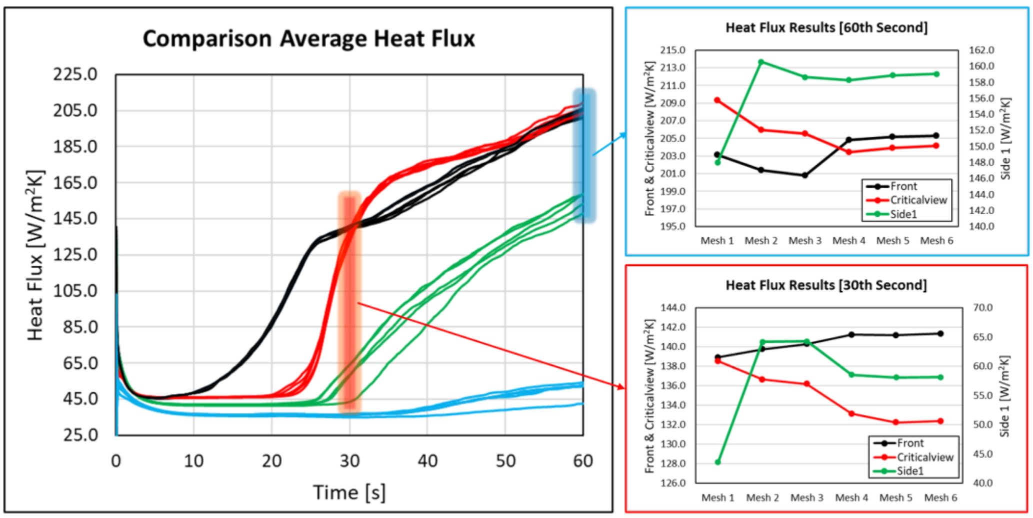

Figure 4. 6 : Heat flux results of mesh independence study

4.3.2. First layer thickness independence study

Since the condensation event occurs directly on the wall surface, the correct resolution of the boundary layer region is critical for the reliability of numerical results. Particularly when using the Eulerian Wall Film model, the initial cell height must be appropriately selected to accurately capture the velocity, temperature, and humidity gradients near the wall. Therefore, in this study, an independence study of the first layer thickness is performed to evaluate the effect of the wall solution on the results.

As shown in Figure 4. 7, the first layer thickness independence study is based on Mesh 4, which is selected as a result of the mesh independence study. Mesh 4 is the optimal mesh structure obtained in the mesh independence study and is used as the medium boundary layer solution in this study. In the meshes from Mesh 5 to Mesh 10, the cell sizes are kept the same as Mesh 4, and only the boundary layer parameters are changed as given in the figure. During this process, attention is paid to keeping the total boundary layer thickness as constant as possible while changing the FLT value. Based on the results obtained, it is determined that the boundary layer structure of Mesh 4 also provides the optimal solution in the first layer thickness independence study.

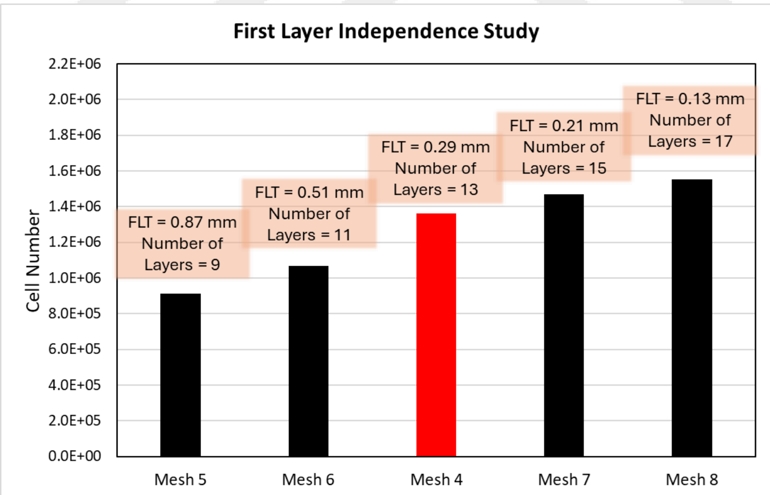

Figure 4. 7 : Cell number of the first layer thickness independence study

Figure 4. 8 presents comparisons of the average heat flux values calculated for different first layer thickness values at 30 and 60 seconds. When examining the results obtained for both time points, it is observed that there are limited changes in heat flux values depending on the first layer thickness variation, but the general trend is similar for all mesh structures. Particularly at Mesh 7 and Mesh 8 levels, more pronounced differences in heat flux values are observed due to the relatively insufficient resolution

near the wall, while it is remarkable that the results are quite close to each other in Mesh 4 and finer boundary layer solutions. After Mesh 4, the change in heat flux values calculated for both the 30th and 60th seconds for the front window and critical viewing area remained quite limited, and it is determined that the transition to thinner first layer thickness values does not provide a significant improvement in thermal results. The results obtained for the side panel also show a similar trend, and the time-dependent behaviour of heat flux is consistently maintained in the solutions after Mesh 4. These findings reveal that first layer thickness independence is achieved at the Mesh 4 level and that this mesh structure adequately represents condensation and heat transfer processes with sufficient accuracy.

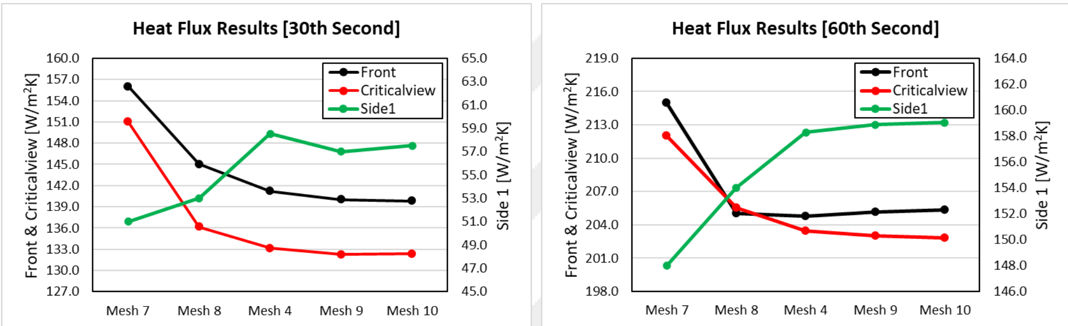

Figure 4. 8 : Heat flux results of first layer thickness independence study

Consistent with the heat flux results, the film mass comparisons presented in Figure 4. 9 also demonstrate that first layer thickness independence is achieved at the Mesh 4 level. At both 30 and 60 seconds, the film mass values calculated for the front window and critical viewing area are seen to be quite close for Mesh 4 and thinner boundary layer solutions. This situation demonstrates that the Mesh 4 grid provides reasonable and sufficient resolution not only in terms of thermal quantities but also in terms of estimating the film mass formed as a result of condensation.

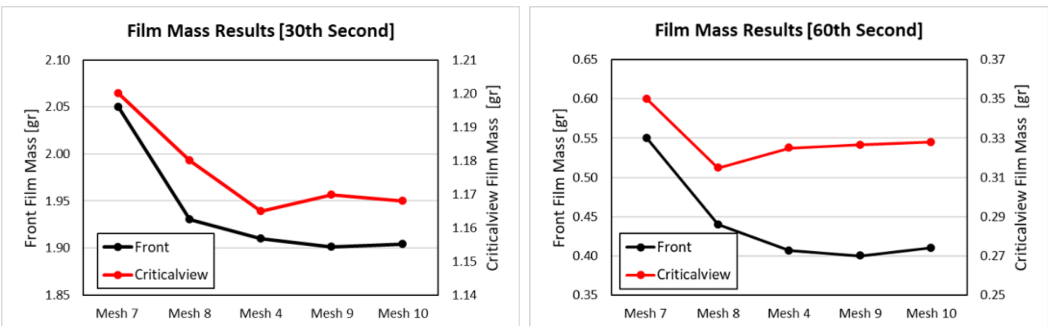

Figure 4. 9 : Film mass results of mesh independence study

4.3.3. Time step independence study

In time-dependent dew point analysis, selecting an appropriate time step is critical for the accuracy and stability of the numerical solution. Selecting a time step that is too large may result in transient flow and condensation processes not being captured with sufficient temporal resolution, while very small time steps significantly increase computational costs. Therefore, a time step independence study is conducted in this study to demonstrate that time-dependent results are independent of the time step.

The time step independence study is carried out in a limited time interval that represents the characteristic behaviour of the time-dependent solution. In this context, all time step comparisons are made over a solution time of 7.5 seconds, and the effect of different time steps on the early-time behaviour is evaluated.

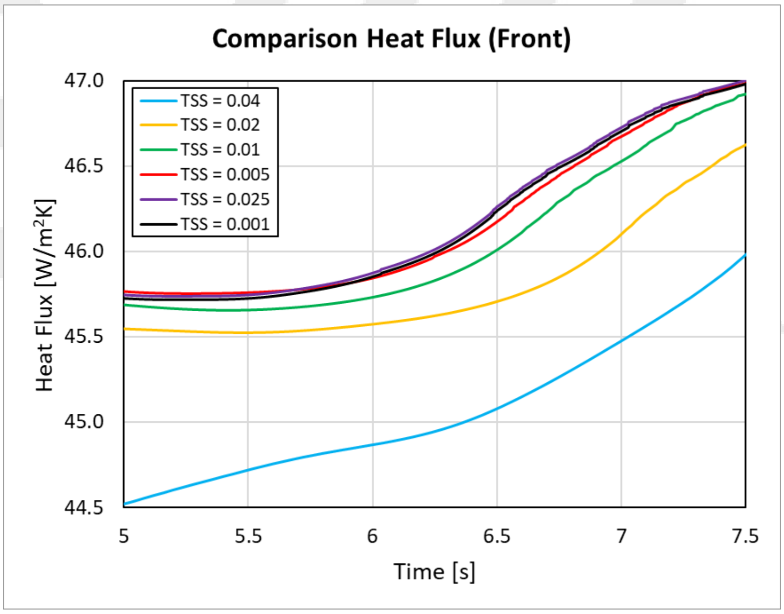

Figure 4. 10 : Heat flux results of time step independence study

Figure 4. 10 presents the time-dependent variation of the heat flux calculated in the front region of the windscreen for different time steps. Analysis of the graph indicates that when large time steps are used (TSS = 0.04 and 0.02), the heat flux values are lower and the temporal trend is different. In contrast, it is observed that the heat flux curves obtained for TSS = 0.01 and smaller time steps are quite close to each other and exhibit similar characteristics in their time-dependent variation. The absence of a noticeable difference between the results for TSS = 0.005 and TSS = 0.001 indicates that the solution becomes independent of the time step within this range. Accordingly, TSS = 0.005 is selected as the final time step for all transient analyses, as it provides

sufficient temporal resolution while keeping computational costs at a reasonable level, and the Courant–Friedrichs–Lewy (CFL) number is maintained below 1 for all cells in the simulations.

4.3.4. Assessment of steady and transient solutions

The Eulerian Wall Film (EWF) model inherently solves condensation and phase change processes as time-dependent. Consequently, film formation, film transport, and vapour-condensation interactions are always addressed within the transient solution framework. In contrast, both steady-state and transient solutions can be applied for the flow field. In this study, based on the findings from mesh, boundary layer, and time step independence studies, cases where the flow field is solved in steady and transient states are compared. The investigations revealed negligible differences between steady and transient flow solutions in terms of the average heat flux and total film mass results on the window surfaces, as shown in Figure 4. 11. This indicates that solving the carrier flow as steady does not significantly affect the accuracy of the results, as the EWF model can capture film and phase change behaviour over time.

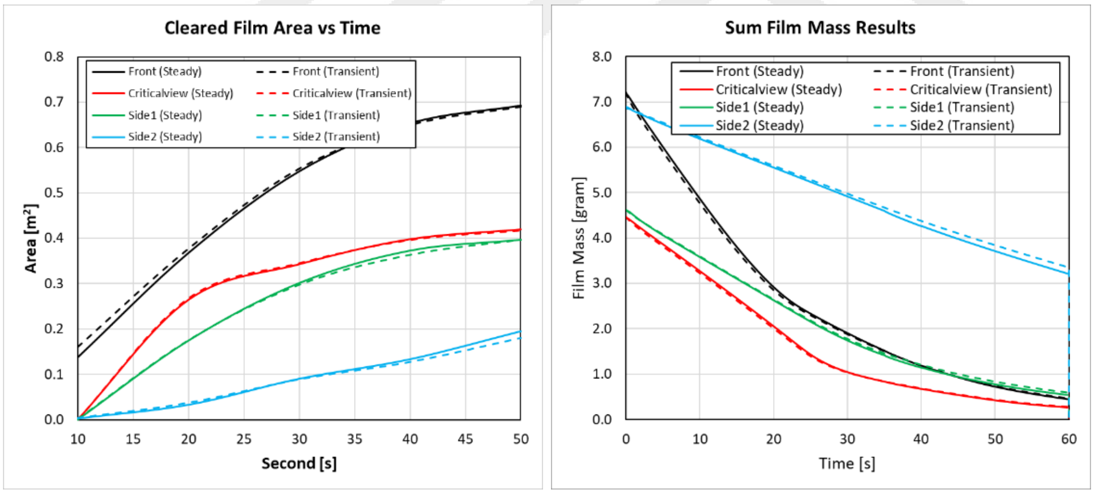

Figure 4. 11 : Steady vs Transient results

Within the EWF model, sub-iterations are always applied at each time step to solve the film equations. When solving the flow field transiently, in addition to these sub-iterations, an inner iteration requirement arises for each time step, significantly increasing the total solution time. In the computational cost comparisons, it was determined that the transient flow solution with a time step of 0.005 s, where the Courant number is below 1, took approximately 3.5 times longer to complete than the steady flow solution. Given that numerous scenarios need to be solved within the scope of regression analyses, the flow field is solved as steady in the final analyses, while the film and phase change processes are solved as transient using the EWF model, in order to keep the computational cost at a reasonable level.

4.4. Definition of Demisting Performance Metrics

In this thesis, the demisting performance of helicopter windshields is evaluated based on metrics representing both the removal of liquid film formed as a result of evaporation and the quality of visibility. In this context, two fundamental quantities are defined for performance evaluation: the total mass of film swept from the windshield surface and the visibility criterion dependent on film thickness, which directly affects visibility on the windshield surface.

As the first metric, the mass of liquid film removed from the windscreen surface during the demisting process is calculated, and this quantity is used as a global performance indicator representing the overall efficiency of the condensation and film transport processes. The swept film mass enables the quantitative comparison of demisting performance under different operating conditions.

As a second metric, the film thickness on the windshield is used to represent visibility safety. In this context, areas where the film thickness remained below the 5 μm visibility threshold at the 60th second of the analyses are identified and defined by their ratio to the total area of the relevant windshield. This approach made it possible to evaluate the demisting process not only in terms of the total film quantity but also in terms of its effect on the pilot's vision.

Using these defined performance metrics, the effects of operating parameters such as inlet air temperature, humidity level and air flow rate on dehumidification performance are examined, and the results obtained are quantitatively evaluated using regression analyses.

4.5. Parametric Study and Regression Analysis

In this section, the effects of operating conditions on demisting performance are examined parametrically within the scope of the demisting analyses conducted for the helicopter windscreen, and the numerical results obtained are evaluated using regression analysis. After establishing the reliability of the numerical model in the previous sections, this section aimed to quantitatively determine the dominant parameters that determine demisting performance under different operating conditions. Thus, the relative importance of the parameters affecting the demisting process is identified, allowing for a more comprehensive evaluation of system behaviour.

Considering that the mist removal performance is fundamentally dependent on the inlet air conditions, the flow rate, temperature, and water vapour mass fraction values of the inlet air are systematically changed in the parametric studies. The inlet air flow rate directly affects the transport mechanisms formed across the windscreen surface, while air temperature and humidity are the fundamental thermodynamic parameters that determine the condensation potential and the amount of film formation. Therefore, based on the demisting performance metrics defined in Definition of Demisting Performance Metrics section, separate regression analyses are performed for both the total swept film mass and the visible area ratio representing pilot visibility, and the effects of inlet air conditions on these two performance metrics are quantitatively investigated.

Due to the helicopter's ability to operate at different altitudes, the effect of operating pressure on demisting performance under the same inlet air conditions is also included in the parametric study. As a result of analyses conducted at different operating pressures representing medium (5000 feet) and high (10.000 feet) altitude conditions, the effects of ambient pressure on both the total film mass and the visible area ratio are evaluated using regression analysis. This allows for a comprehensive demonstration of how altitude variation affects demisting performance, in addition to inlet air conditions, through two different performance metrics.

Within this scope, the flight and operating conditions selected for use in regression analyses are summarised in Table 4. 1. The conditions given in the table are determined to include representative combinations of parameters such as inlet air flow rate, temperature, humidity, and operating pressure, and are designed to enable the systematic investigation of the fundamental parameters affecting demisting performance. The results obtained from the numerical analyses performed under these specified flight conditions are used in the regression studies presented in the following subheadings.

Table 4. 1 : Inlet conditions of the regression cases

Analysis Case No	Mass Flow Rate [kg/s]	Temperature [°C]	Mass Fraction	Relative Humidity	Pressure Altitude
Case 1	0.10	55	0.0015	4%	5000 Feet
Case 2	0.10	55	0.00484	14%	
Case 3	0.50	20	0.0015	12%	
Case 4	0.50	20	0.00484	38%	
Case 5	0.50	55	0.0015	4%	
Case 6	0.50	55	0.00484	14%	
Case 7	0.16	48	0.002669	9%	
Case 8	0.20	30.5	0.004506	28%	
Case 9	0.24	41	0.001834	8%	
Case 10	0.28	25.25	0.003337	26%	
Case 11	0.32	53.25	0.004005	12%	
Case 12	0.36	35.75	0.002335	14%	
Case 13	0.40	44.5	0.004673	20%	
Case 14	0.44	27	0.001667	12%	
Case 15	0.14	37.5	0.003671	24%	
Case 16	0.46	49.75	0.002836	9%	
Case 17	0.28	25.25	0.003337	26%	
Case 18	0.4	44.5	0.004673	20%	
Case 19	0.18	46	0.00355	13%	
Case 20	0.26	51	0.00195	6%	
Case 21	0.3	34	0.0029	18%	
Case 22	0.34	39	0.00325	18%	
Case 23	0.38	27.5	0.00205	15%	
Case 24	0.42	54	0.00385	11%	
Case 25	0.48	43	0.00275	12%	
Case 26	0.16	47	0.00435	17%	
Case 27	0.1	55	0.00150	4%	10.000 Feet
Case 28	0.1	55	0.00484	14%	
Case 29	0.5	20	0.00150	12%	
Case 30	0.5	20	0.00484	38%	
Case 31	0.5	55	0.00150	4%	

Table 4. 2 (continued) : Inlet conditions of the regression cases

Analysis Case No	Mass Flow Rate [kg/s]	Temperature [°C]	Mass Fraction	Relative Humidity	Pressure Altitude
Case 32	0.5	55	0.00484	14%	10.000 Feet
Case 33	0.16	48	0.00267	9%	
Case 34	0.2	30.5	0.00451	28%	
Case 35	0.24	41	0.00183	8%	
Case 36	0.32	53.25	0.00401	12%	
Case 37	0.36	35.75	0.00234	14%	
Case 38	0.4	44.5	0.00467	20%	
Case 39	0.44	27	0.00167	12%	
Case 40	0.14	37.5	0.00367	24%	
Case 41	0.46	49.75	0.00284	9%	
Case 42	0.4	44.5	0.00467	20%	

4.5.1. Regression analysis based on total cleared film mass

In this study, the total film mass swept away in 60 seconds is considered as a global performance metric representing demisting performance, and its relationship with the inlet conditions is investigated using regression analysis. Within the parametric study, inlet mass flow rate, inlet air temperature, and inlet air mass fraction are determined as independent variables. The combined effects of these parameters on the transport, thinning, and removal of the liquid film on the windshield surface are evaluated using a regression model developed from CFD results. Thus, the aim is to quantitatively identify the dominant parameters governing the demisting process and their relative effects.

The CFD data used in the regression analysis are obtained under the flight conditions presented in Table 4. 1. These conditions are selected to cover the specified parameter ranges and are arranged to form a working space that can represent the effects of different mass flow rates, temperatures, and humidity levels on demisting performance. Thus, the regression model is based not only on limited points but on a wide combination of parameters representing the relevant flight conditions.

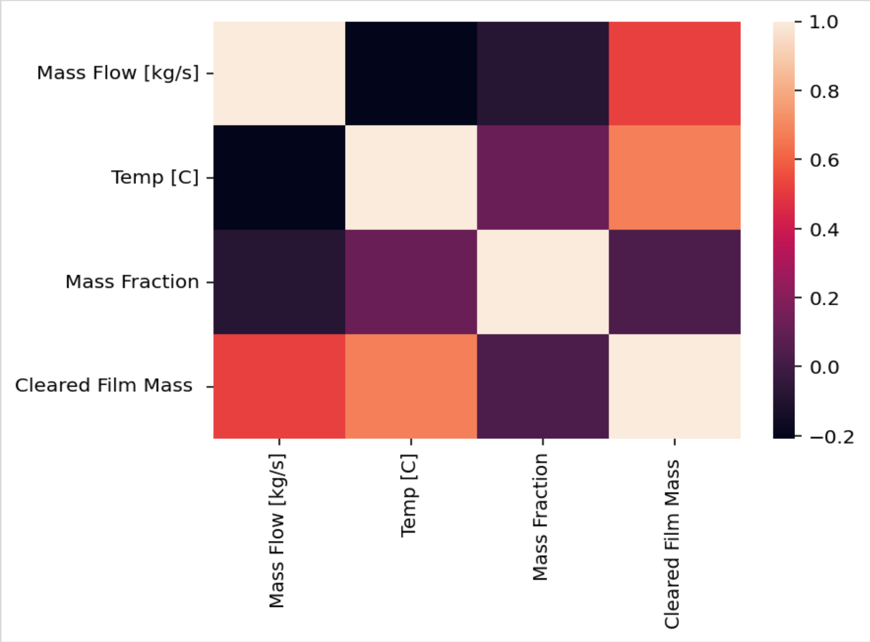

Figure 4. 12 : Regression map of cleared total film mass for three parameters

When the regression analysis results are evaluated using the regression-based relationship map provided in Figure 4. 12, it is observed that the inlet air temperature has the most dominant effect on the total cleaned film mass. The fact that the relationship between temperature and cleaned film mass has higher normalised values on the map indicates that temperature plays a decisive role in explaining the demisting performance. Mass flow rate emerges as the second most influential parameter due to the mechanical sweeping effect, while the regression model assigns a higher sensitivity to the temperature variable when explaining the output. This is consistent with the structure of regression analysis, which evaluates the simultaneous effects of parameters.

The limited effect of the moisture mass fraction on the total cleaned film mass observed in the regression results should not be interpreted as meaning that relative humidity is insignificant in the demisting process. The moisture mass fraction is an absolute indication of relative humidity, which is a parameter directly dependent on temperature. Therefore, increases in temperature indirectly affect the relative humidity level and reduce the tendency to condense. Consequently, the prominence of temperature as a dominant parameter in the regression analysis does not mean that the effect of relative humidity is completely eliminated; on the contrary, it shows that the effect of humidity is indirectly reflected in the model through temperature.

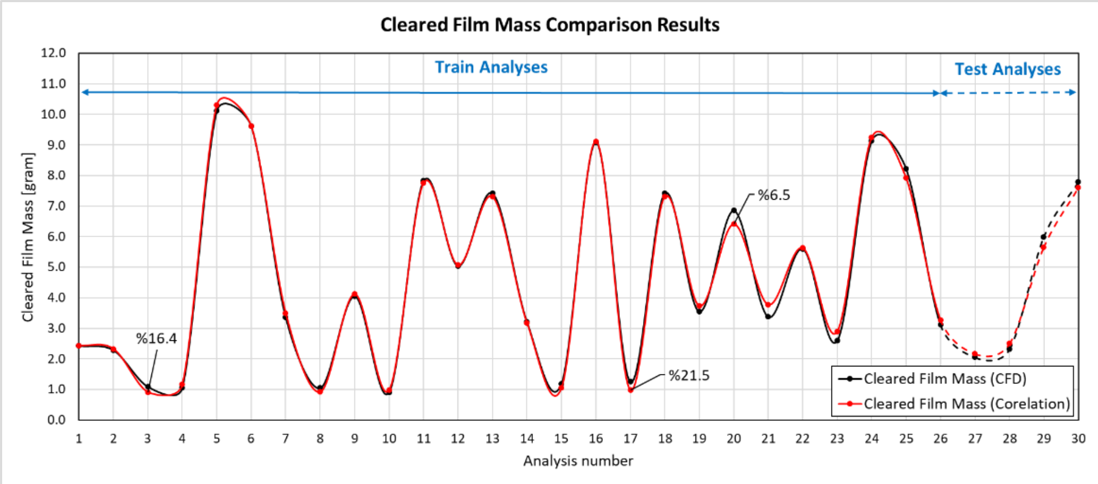

Figure 4. 13 : Cleaned film mass results of CFD and regression correlation for three parameters

The accuracy and applicability of the regression model are evaluated by comparing the CFD results with the regression outputs. In this context, 26 of the total 30 analysis sets are used for training the regression model, while 4 analysis sets are separated for testing purposes without being included in the model. Figure 4. 13 presents both the cleaned film mass values obtained by CFD results and the results predicted by the regression model. In the analyses belonging to the training set, the regression model closely follows the CFD results with high accuracy, while in the test analyses, the model successfully captures the general trend. The R^2 coefficient for the obtained regression model is calculated as 0.99, indicating that the model can represent the total cleaned film mass with high accuracy. The regression correlation equation is

$$35.59\,\dot{m} + 0.47\,T + 848.13\,Y - 34.99\,\dot{m}^2 + 0.11 * \dot{m} * T - 437.65 * \dot{m} * Y$$
$$-0.0033\,T^2 - 8.12 * T * Y - 61588\,Y^2 - 17.89 \;= \text{Cleared Film Mass} \qquad (4.1)$$

In the comparison analysis, the highest relative error rate of 21.5% was observed for Case 17. However, this is related to the fact that the absolute value of the swept film mass in the relevant analysis is quite low. When the film mass is small, it is expected that the relative error rate will appear high despite the limited absolute difference. In contrast, in analyses where the swept film mass is higher, the error rates of the regression model are seen to decrease significantly. For example, for Case 20, the error rate remained at only 6.5%. These results demonstrate that the regression model provides reliable estimates, particularly in high film mass ranges where demisting performance is more critical from an engineering perspective.

Considering the overall results, the regression model demonstrated strong agreement with CFD results for both training and test analyses; it also showed that the model could produce consistent predictions on independent test data. This indicates that the developed regression approach can be used as a reliable tool for the rapid assessment of demisting performance and for making predictions under different operating conditions.

Helicopter operations are conducted not under fixed environmental conditions, but under varying atmospheric conditions at different altitudes. With changes in altitude, the operating pressure value of the flow field around the helicopter changes; consequently, air density, viscosity, and other thermophysical fluid properties are directly affected. These changes indirectly alter demisting performance by affecting both the flow characteristics developing along the windshield surface and the liquid film behaviour. Therefore, a regression model created only with the inflow mass flow rate, temperature, and humidity parameters may be insufficient to fully represent the helicopter's actual operating conditions.

To account for this situation, the effect of operating pressure on altitude is also included in the regression analysis. Within this scope, operating pressure values of 84,500 Pa and 69,700 Pa for helicopter operation at 5,000 ft and 10,000 ft altitudes, respectively, were added to the regression model; thus, the number of independent variables increased to four. The relationships between the total cleaned film mass obtained from this expanded regression model, which considers the input mass flow rate, temperature, moisture mass fraction, and operating pressure parameters together, are analysed using the regression-based relationship map presented in Figure 4. 14.

The regression relationship map presented in Figure 4. 14 reveals the relative importance of the variables affecting the total cleaned film mass, including the operating pressure parameter. According to the map, it is observed that, consistent with previous regression results, the inlet air temperature has the strongest positive relationship with the cleaned film mass. While mass flow rate follows as the second most dominant parameter due to the mechanical sweeping effect, the fact that temperature remains the most decisive variable indicates that the demisting process is strongly dependent not only on fluid transport but also on thermodynamic processes.

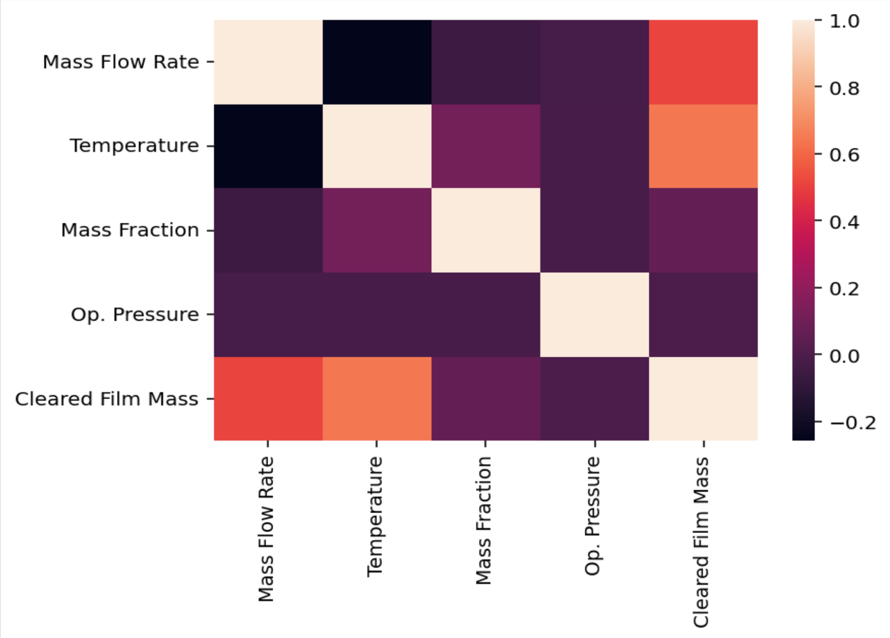

Figure 4. 14 : Regression map of cleared total film mass for four parameters

It is observed that the relationship between the operating pressure parameter and the cleaned film mass remains relatively weak. This situation indicates that operating pressure does not directly determine demisting performance as a parameter, but rather has an indirect effect through the thermophysical properties of the fluid, such as density and viscosity. In this study, the heat transfer coefficient on the helicopter window was kept constant in order to isolate the relative effects of the parameters influencing demisting performance. This approach is a considered choice to enable the effects of the parameters examined in the regression analysis to be distinguished from one another. The regression results indicate that the effect of the operating pressure parameter on the total mass of film removed is limited in relation to altitude changes. However, this does not imply that altitude is insignificant in terms of demisting performance.

Changes in altitude cause variations in the fluid's density and characteristic Reynolds numbers; this affects the flow regime and consequently the external heat transfer coefficient values that may occur. However, the aim of the present study is not to examine the helicopter's behaviour at the same speeds and flow regimes, but rather to evaluate the effect of altitude-induced pressure changes on demisting performance under equivalent heat transfer conditions. In this context, the regression map clearly shows that the effect of operating pressure on demisting performance remains secondary under the assumption of constant external heat transfer coefficient. Therefore, the results obtained represent a controlled and comparable analysis framework rather than a situation detached from physical reality.

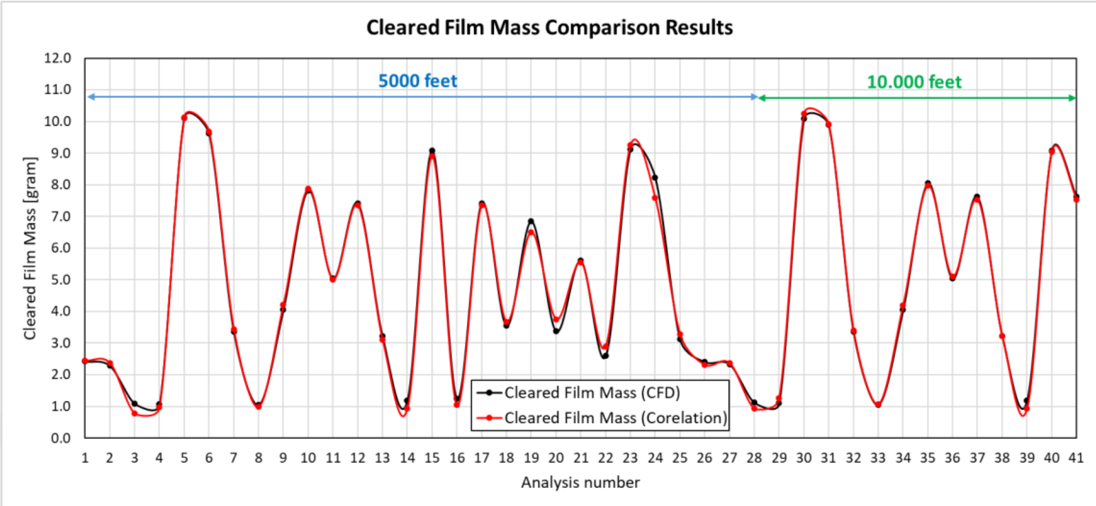

Figure 4. 15 : Cleaned film mass results of CFD and regression correlation for four parameters

The comparison of the results obtained for the four-parameter extended regression model, which also includes the operating pressure parameter, with the CFD data is presented in Figure 4. 15. This comparison is based on analysis sets covering altitude conditions of 5000 ft and 10 000 ft. In the figure, the general trend of the cleaned film mass values calculated by CFD and the results predicted by the regression model show a high degree of agreement. Despite the analyses for different altitude regions being presented on the same graph, it is observed that the regression model successfully follows the CFD results . This indicates that incorporating the operating pressure parameter into the model enhances the regression approach's ability to represent different altitude conditions.

The R^2 value for the developed four-parameter regression model is 0.985, indicating that the model can represent the total cleaned film mass with high accuracy. The small deviations observed in Figure 4. 15 are related to the increase in relative error rates, particularly in analyses where the swept film mass is low. However, considering that the absolute error levels are limited, this situation does not adversely affect the reliability of the model in terms of engineering applications. At high film mass levels, the agreement between the regression model and the CFD results is significantly strengthened.

The total cleaned film mass obtained in this regression analysis is represented by the following expression, which includes the second-order terms and cross-interactions of the input parameters:

$$
\begin{aligned}
&40.96\,\dot{m} + 0.41\,T + 538.26\,RH + 7.51 \cdot 10^{-7}\,Y - 41.72\,\dot{m}^2 + 0.13 * \dot{m} * T \\
&-284.62 * \dot{m} * RH - 3.94 \cdot 10^{-5} * \dot{m} * Y - 0.0028\,T^2 - 5.62 * T * RH + \\
&1.05 \cdot 10^{-7} * T * Y + 3.55\,RH^2 - 0.0027 * RH * Y + 6.65 \cdot 10^{-11} * Y^2 - 16.81 \\
&= \text{Cleared Film Mass}
\end{aligned}
\tag{4.2}
$$

These results demonstrate that demisting performance evaluation based on total film mass can be predicted quickly and reliably.

4.5.2. Regression analysis based on visible area clearance ratio

In evaluating demisting performance, using only a global metric such as the total mass of film swept may not always be sufficient. Although a decrease in total film mass may indicate that the liquid film on the window surface has generally thinned or been removed, this does not necessarily mean that the pilot's view has been effectively cleared. Particularly in areas where the film thickness remains above a certain threshold value, the field of view may remain limited even if the total film mass has decreased. Therefore, in order to evaluate demisting performance in a more operationally meaningful way, it is necessary to consider areas on the windscreen surface where the film thickness is below a certain critical 5μm value as determined in Section 1.2.3.

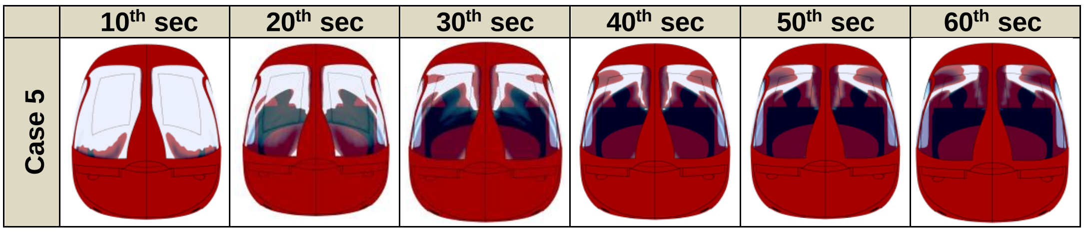

Figure 4. 16 : Time-dependent development of the visible area for Case 5

According to the film mass regression analysis, Case 5 exhibited the highest demisting performance. For Case 5, the time-dependent development of the mist distribution on the windshield surface is examined at 10-second intervals, and the results are presented in Figure 4.16. In this analysis, areas where the film thickness fell below the critical threshold value of 5 µm were defined as the visible area. Although the liquid film on the windshield surface generally thinned as time progressed, it is clear that the removal of fog did not occur uniformly across the surface. While the film in some areas is completely removed, opening up the field of view, liquid accumulation continues in some areas. This situation demonstrates that demisting performance cannot be fully represented by looking only at the total mass of film swept away.

In this section, the regression used in the previous section is reapplied with the same input parameters to evaluate demisting performance using a vision-based performance metric. In this context, inlet mass flow rate, inlet air temperature, and inlet air mass fraction are selected as independent variables; the ratio of the areas where the film thickness on the windshield surface falls below the critical threshold value of 5 µm (from 10 µm) to the total windshield area is defined as the dependent variable in the regression model output. This ratio represents the areas where the view is effectively opened due to the decrease in film thickness and allows the demisting performance to be evaluated directly in terms of pilot visibility. Thus, the functional outputs of the demisting process are examined using regression analysis, which goes beyond a purely mass-based approach.

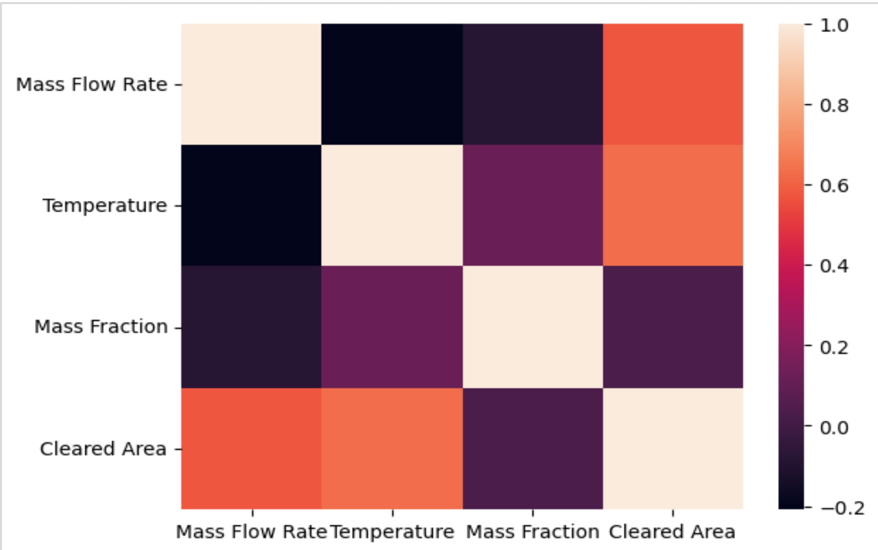

Figure 4. 17 : Regression map of clearance area ratio for three parameters

The regression relationship map presented in Figure 4. 17 reveals the relative relationships between the visible area ratio and the input parameters. When the map is examined, it is seen that the input air temperature has the most dominant effect on the visible area ratio. The strong positive relationship between temperature and visible area indicates that thermodynamic mechanisms play a decisive role in the film thickness falling below the critical threshold value. This result is directly consistent with the findings obtained in the regression analysis based on the total swept film mass in the previous section and once again confirms that temperature is the dominant parameter in demisting performance. While temperature and mass flow rate are the dominant parameters in both performance metrics, the effect of moisture mass fraction remains secondary. However, due to the visible area ratio being more sensitive to local variations in film thickness, this metric provides a complementary and functional assessment in terms of representing the pilot view.

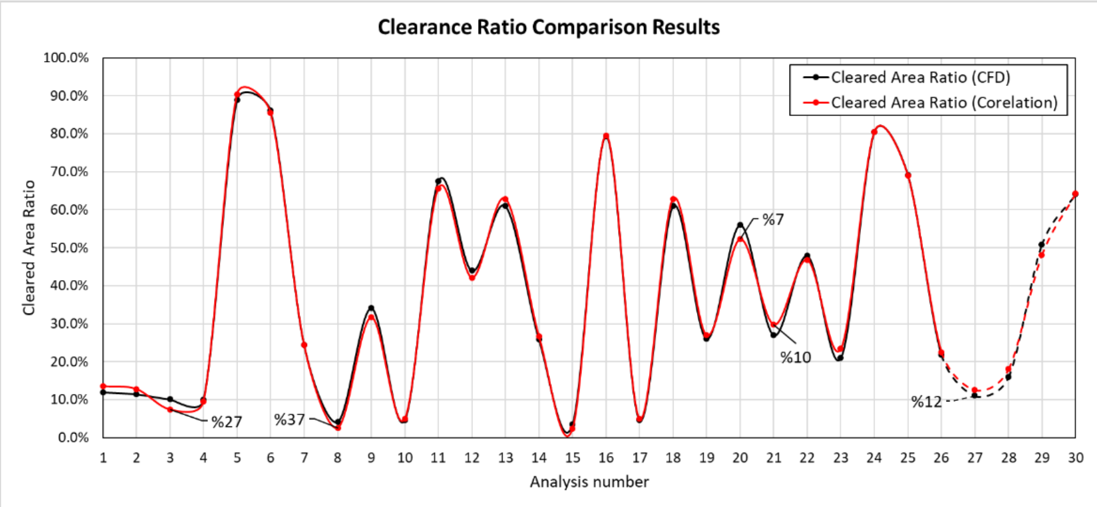

Figure 4. 18 : Clearance area ratio results of CFD and regression correlation for three parameters

Figure 4. 18 presents a comparison of CFD results with regression model outputs for the cleared area ratio. The graph shows that the regression model successfully follows CFD results in terms of general trend in both training analyses and independent test analyses. The highest relative error rates occur in analyses where the cleared area ratio is low; however, this is due to the sensitivity of the relative error definition, despite the limited absolute area differences. In contrast, the agreement between regression estimates and CFD results increases significantly in analyses where the cleared area ratio is high. Overall, the regression model reliably represents the time-dependent and parameter-sensitive variation of the visible area ratio.

The visible area ratio obtained in this regression study is defined by the following second-order expression, which includes the parameters of inlet mass flow rate ($\dot{m}$), temperature (T) and mass fraction of moisture (Y):

$$3.34\,\dot{m} + 0.04\,T + 66.22\,Y - 3.26\,\dot{m}^2 + 0.011 * \dot{m} * T - 30.37 * \dot{m} * Y$$
$$-0.00027\,T^2 - 0.59 * T * Y - 5192.2\,Y^2 - 1.623 = \text{Cleared Area Ratio} \quad (4.3)$$

For 30 analysis sets, contour images of the areas where the film thickness on the windshield surface falls below the critical threshold value of 5 μm at the 60th second of the demisting process are presented in Figure 4.19. The contours shown reveal the spatial distribution of the visible area under different input conditions and demonstrate that demisting performance exhibits significant differences not only in terms of magnitude but also in terms of the local spread characteristics on the surface.

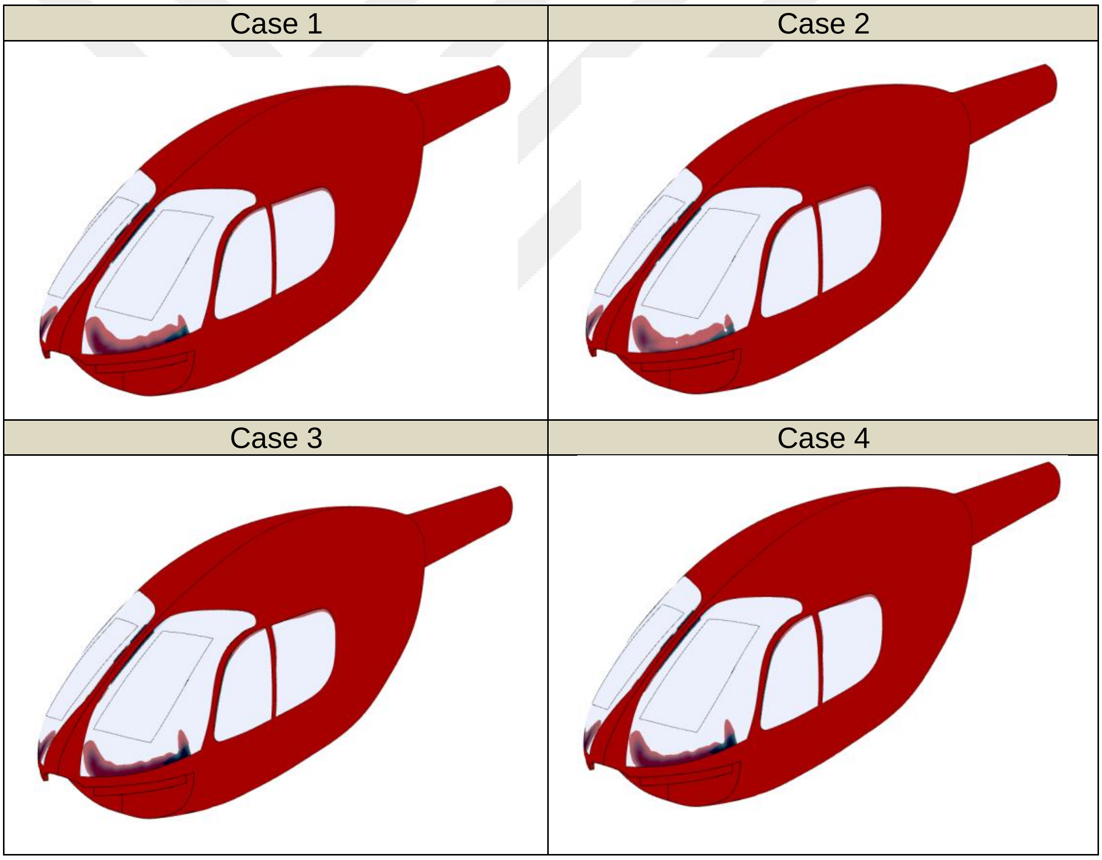

Figure 4. 19: Visible area contours at 5 μm critical film thickness at 60 seconds for 30 analysis sets

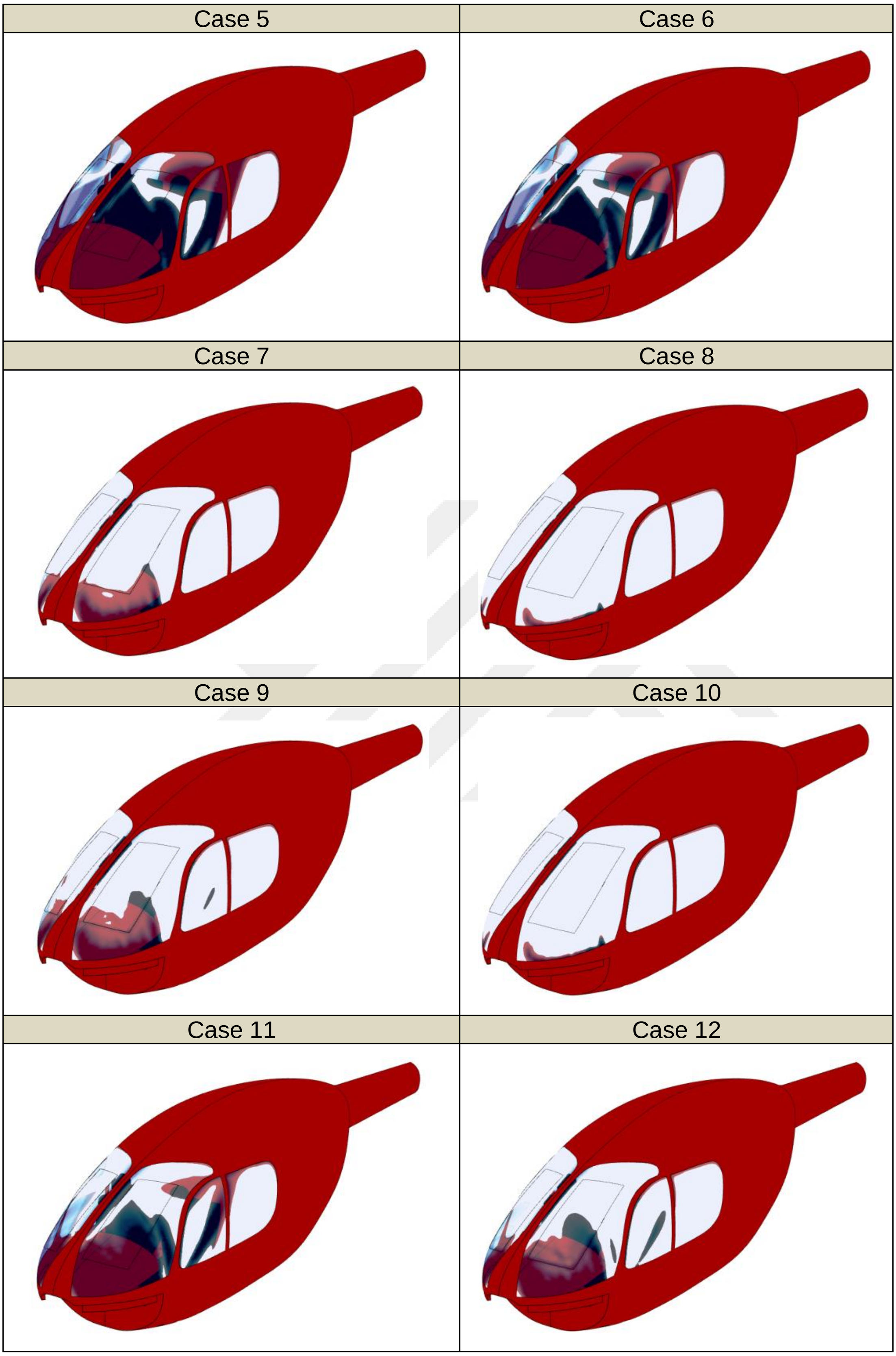

Figure 4. 19 (continued): Visible area contours at 5 µm critical film thickness at 60 seconds for 30 analysis sets

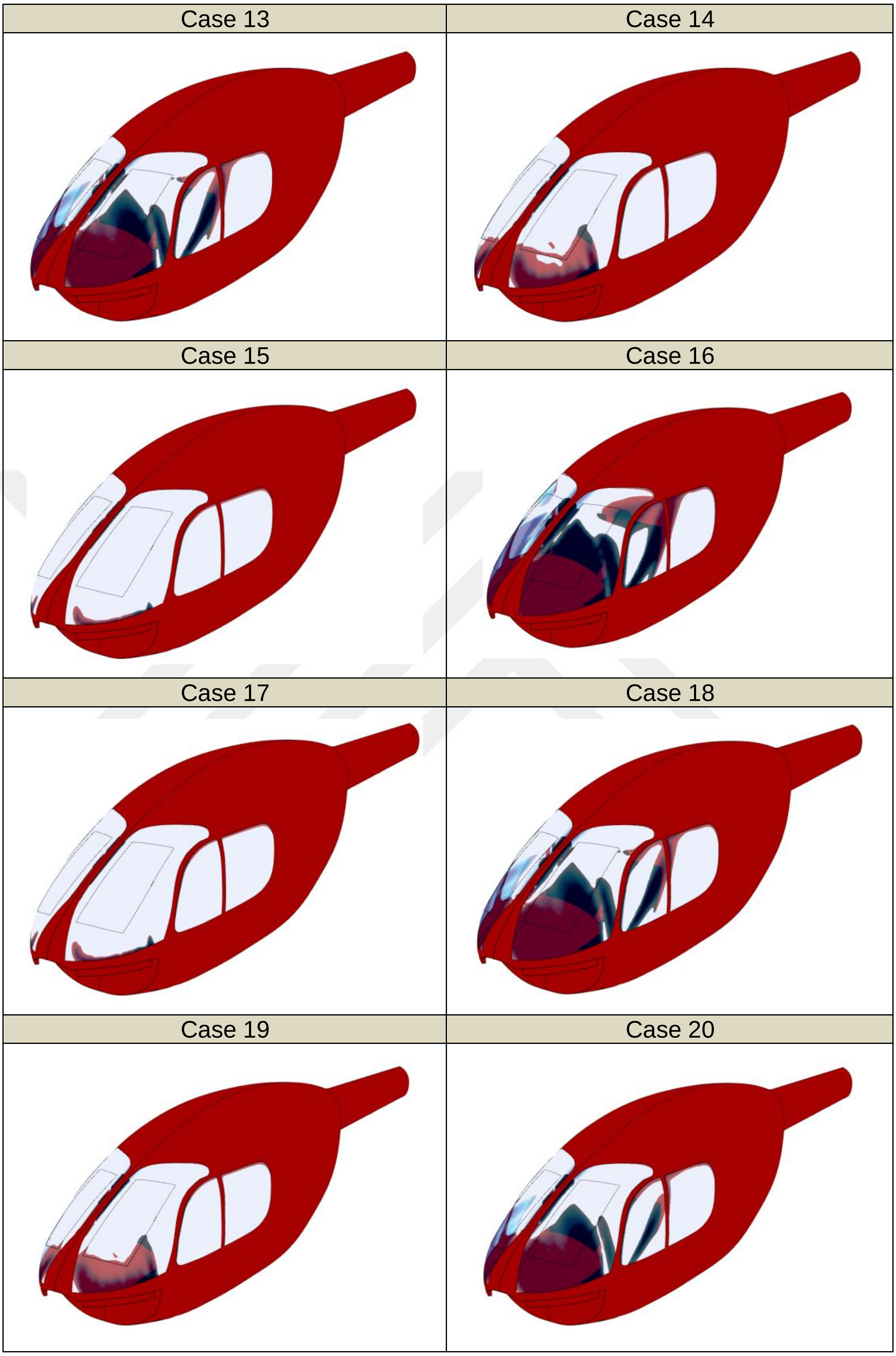

Figure 4. 19 (continued): Visible area contours at 5 μm critical film thickness at 60 seconds for 30 analysis sets

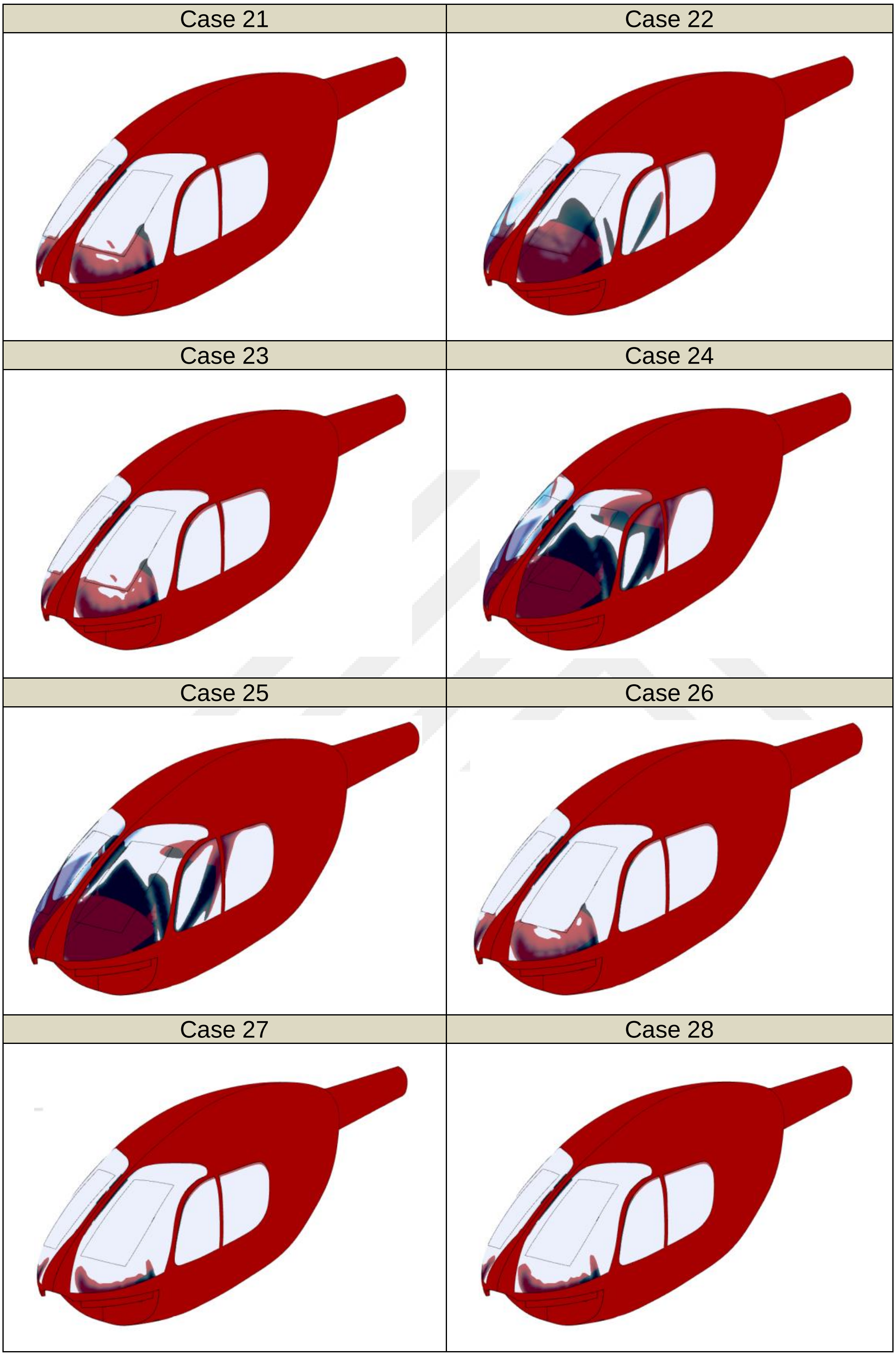

Figure 4. 19 (continued): Visible area contours at 5 µm critical film thickness at 60 seconds for 30 analysis sets

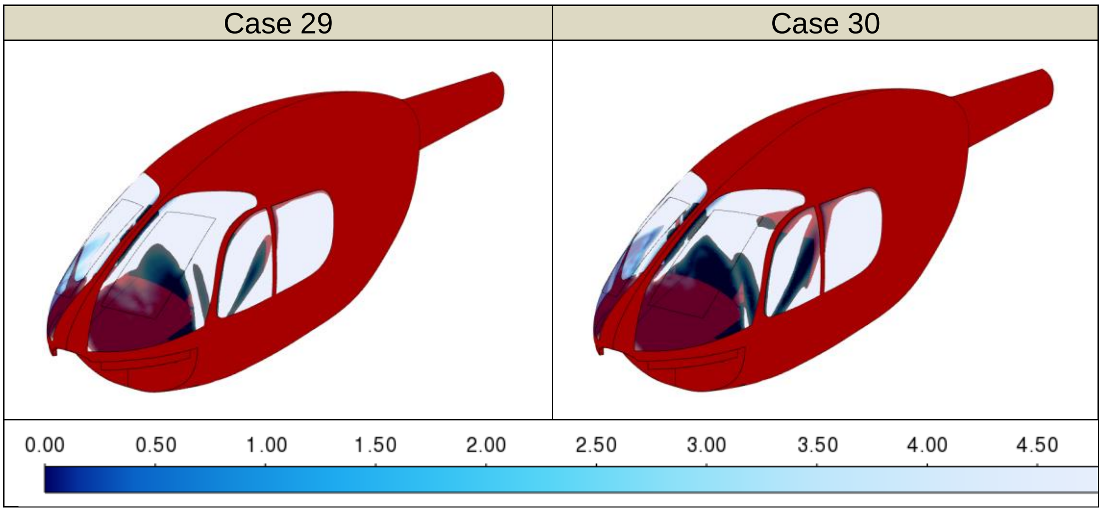

Figure 4. 19 (continued): Visible area contours at 5 μm critical film thickness at 60 seconds for 30 analysis sets

4.6. Discussion of Results

The inlet air temperature is the most dominant parameter in the demisting process for both performance metrics. As the temperature increases, the tendency for condensation on the window surface decreases and the evaporation potential of the existing liquid film increases. In addition, temperature plays a directly decisive role on relative humidity; under constant absolute humidity conditions, an increase in temperature causes a decrease in relative humidity and the dew point temperature to move away from the window surface temperature. This situation contributes to both a reduction in the total film mass and a faster drop in film thickness below the critical threshold value. Therefore, temperature is the fundamental determining parameter in both mass-based and vision-focused demisting metrics.

Mass flow rate primarily affects demisting performance through mechanical transport and shear stresses formed along the surface. Increasing flow rate raises flow velocities across the windshield surface, facilitating the transport and local thinning of the liquid film. However, not only the magnitude of the flow rate but also the access area and direction of the flow on the windshield surface are important for demisting. The concentration of flow in certain areas causes some areas to clear more quickly, while film accumulation may continue in other areas. Therefore, while mass flow rate is a strong parameter, particularly in terms of total swept film mass, it exhibits a more balanced effect in terms of the visible area ratio metric.

The mass fraction of moisture shows a limited direct effect on both performance metrics in regression analyses. However, this result should not be interpreted as meaning that moisture is insignificant in the demisting process. The mass fraction of moisture is an absolute expression of relative humidity, and its effect on the condensation behaviour of relative humidity on the window surface should be evaluated in conjunction with temperature. As seen in this study, the effect of humidity mostly emerges interactively with temperature; it indirectly influences film formation and dissolution processes, particularly through relative humidity and dew point temperature. Therefore, the humidity parameter plays a meaningful role in demisting physics when considered together with temperature, rather than alone.

The altitude effect is represented by operating pressure in this study. With altitude changes, thermophysical fluid properties such as air density and viscosity change; this indirectly affects the demisting process. However, in the current analyses, the heat transfer coefficient on the window surface is kept constant, and the altitude effect is isolated under equivalent heat transfer conditions. Under this approach, the effect of operating pressure variation on demisting performance is found to be limited. In actual flight conditions, however, changes in the Reynolds number associated with altitude variation and the resulting changes in the heat transfer coefficient may also play a significant role; however, this effect is beyond the scope of the present study.

When taken together, the total swept film mass and visible area ratio metrics represent demisting performance from different but complementary perspectives. While temperature and mass flow rate are the dominant parameters for both metrics, the visible area ratio metric provides a more sensitive assessment of local variations in film thickness. Therefore, it has been concluded that considering both metrics together is necessary and beneficial for accurately evaluating demisting performance from both a global and operational perspective.

5. FINDINGS AND RECOMMENDATIONS

Within the scope of this thesis, the performance of demisters aimed at eliminating fogging problems on helicopter windshields is examined using computational fluid dynamics (CFD)-based analyses and regression methods. In the first stage of the study, the Eulerian Wall Film (EWF) model and the species transport approach are used together in order to accurately model condensation and liquid film dynamics. The numerical model developed exhibited physical behaviour consistent with similar condensation and film transport studies in the literature, successfully capturing heat and mass transfer physics with an error rate below 10%.

The developed CFD model is examined through the swept film mass and areas opened depending on the film thickness obtained throughout the demisting process. In the study, two independent performance metrics enabling the evaluation of demisting performance from both a mass and visual perspective are defined and analysed parametrically. The main findings are summarised below:

- ✓ To evaluate the demister performance, two separate performance metrics have been defined: the total liquid film mass swept within 60 seconds and the ratio of the total viewing area to the area where the film thickness falls below 5 microns. This approach provides a metric that directly represents pilot viewing quality, rather than just a mass-based evaluation.
- ✓ In parametric studies conducted using inlet air mass flow rate, temperature, and water vapour mass fraction parameters, temperature is found to be the most dominant parameter for both performance metrics. Increased air temperature reduced the amount of condensation by improving dew point conditions and significantly increased both the swept film mass and the visible area ratio.
- ✓ Air flow rate is an important parameter, particularly in terms of the spread of flow along the window surface and the transport of the liquid film. However, the effect of flow rate is secondary to temperature and should be evaluated in conjunction with geometric flow characteristics.

- ✓ It is determined that the direct effect of water vapour mass fraction on regression results is limited. However, this finding does not imply that relative humidity is insignificant. On the contrary, it is observed that relative humidity plays a critical role in demister performance when evaluated together with temperature, particularly in determining the initial condensation conditions.
- ✓ The operating pressure values, which vary depending on the helicopter's operating altitude, are included in the regression analyses and the number of parameters is expanded to four. In this context, it is observed that the effect of altitude change on demisting performance is limited under constant heat transfer coefficient conditions. However, considering that the Reynolds number and consequently the heat transfer coefficient will change with altitude under real operational conditions, it is assessed that this effect may indirectly increase.
- ✓ The developed regression models are compared with CFD results and show high agreement for both training and test data sets. It is determined that the R^2 values of the regression models obtained for the total swept film mass and visible area ratio are in the range of 0.98–0.99, while the maximum error rates are found to increase relatively at low film mass levels. This situation stems from the increase in proportional errors despite the small absolute differences.

The findings obtained as a result of this study clearly demonstrate the necessity of using multiple performance metrics in the evaluation of helicopter demist performance. The proposed regression approach offers fast and reliable predictions at a lower computational cost compared to CFD analyses and can be used as an effective tool in early design stages and system optimisation studies.

Recommendations for Future Work:

- By including the heat transfer coefficient, which varies with altitude, in regression models, it is possible to examine more realistic operational scenarios.
- By investigating the role of rotor-induced flow effects on demisting performance, results closer to actual flight conditions can be obtained.

- By performing similar parametric and regression analyses for different window surfaces and airflow configurations, the generalisability of the results can be increased.
- The defined visible area ratio metric can be linked to pilot visual quality and supported by human factors-based studies.

REFERENCES

[1] **Cengel, Y. A., Ghajar, A. J.,** (2015) Heat and Mass Transfer: Fundamentals and Applications. Fifth Edition.

[2] **Incropera, F. P., DeWitt, D. P., Bergman, T. L., Lavine, A. S.,** (2007) Fundamentals of Heat and Mass Transfer. Sixth Edition.

[3] **Ghiaasiaan, S. M.,** (2007) Two-Phase Flow, Boiling, and Condensation: In Conventional and Miniature Systems. Cambridge University Press.

[4] **Moran, M. J., Shapiro, H. N., Boettner, D. D., Bailey, M. B.,** (2018) Fundamentals of Engineering Thermodynamics. Ninth Edition.

[5] **Guzej, M., Zachar, M.,** (2019) CFD Simulation of Defogging Effectivity in Automotive Headlamp. Energies, Vol. 12, No. 13, 2609.

[6] **ASHRAE,** (1992) ASHRAE Psychrometric Chart No. 1: Normal Temperature, Sea Level. American Society of Heating, Refrigerating and Air-Conditioning Engineers.

[7] **Bhowmik, P. K., Ormiston, S. J., Schlegel, J. P., Chowdhury, D.,** (2023) State-of-the-art and review of condensation heat transfer for small modular reactor passive safety: Computational studies. Nuclear Engineering and Design, Vol. 410, 112366.

[8] **Ambrosini, W., Bucci, M., Forgione, N., Jahn, W., et al.,** (2008) Comparison and Analysis of the Condensation Benchmark Results. Nuclear Engineering and Design.

[9] **Panfilov, I., Beskopylny, A. N., Meshki, B., Podust, S. F.,** (2025) Numerical Study of Gas Dynamics and Condensate Removal in Energy-Efficient Recirculation Modes in Train Cabins. Fluids, Vol. 10, No. 8, 197.

[10] **Mehdipour, R., Baniamerian, Z., Saidi, M. H.,** (2017) A New Approach in Developing Optimal Defrost/Demist Performance in a Passenger Car. International Journal of Engineering, Vol. 30, No. 7, 1081–1089.

[11] **Yang, Y., Huang, Y., Zhao, J.,** (2020) Optimization of the automotive air conditioning strategy based on the study of dewing phenomenon and defogging progress. Applied Thermal Engineering, Vol. 169, 114932.

[12] **Federal Aviation Administration (FAA),** (2016) 14 CFR 29.773 – Pilot Compartment View. Code of Federal Regulations, United States.

[13] **Federal Aviation Administration (FAA),** (2012) FAA AC 25.773-1 – Pilot Compartment View Design Considerations. Advisory Circular, United States.

[14] **Hassan, Y., et al.,** (1999) Windshield Defogging Simulation with Comparison to Test Data 1999-01-1202. SAE Technical Paper.

[15] **ANSYS Inc.,** (2025) ANSYS Fluent Theory Guide. Release 2025 R2.

[16] **Koca, A.,** (2015) Düşey Bir Plaka Yüzeyinde Doğal Taşınım Şartlarında Yoğuşmanın İncelenmesi. Doktora Tezi, Yıldız Teknik Üniversitesi, İstanbul.

[17] **Comini, G., Savino, S.,** (2007) Latent and Sensible Heat Transfer in Air Cooling Application. International Journal of Numerical Methods for Heat and Fluid Flow, Vol. 17, 608–627.

[18] **Siemens Digital Industries Software,** (2018) STAR-CCM+ Theory Guide. Version 13.04.

[19] **Schlichting, H., Gersten, K.,** (2017) Boundary-Layer Theory. Ninth Edition.

[20] **Ambrosini, W., Forgione, N., Merli, F., et al.,** (2014) Lesson learned from the SARNET wall condensation benchmarks. Annals of Nuclear Energy, Vol. 74, 153–164.

[21] **Dai, Qiumin, Fang, Xiande,** (2016) Numerical study of forced convective heat transfer around airships. Advances in Space Research, Vol. 57, No. 3, 776–781.

CURRICULUM VITAE

Name Surname : Furkan KESIM

EDUCATION :

• B.Sc. **:** 2021, Yıldız Technical University, Faculty of Mechanical Engineering, Department of Mechanical Engineering

PROFESSIONAL EXPERIENCE AND REWARDS:

• 2021 – Present: Senior Specialist Thermal & CFD Engineer, Helicopter Department, Turkish Aerospace

PUBLICATIONS, PRESENTATIONS AND PATENTS ON THE THESIS:

• **Kesim F.**, Koca A. 2025. Numerical Validation Of Wall Condensation Phenomenon And Numerical Analysis Of The Helicopter Demisting Performance, November 27-29, 2025 Kyrenia, TRNC.